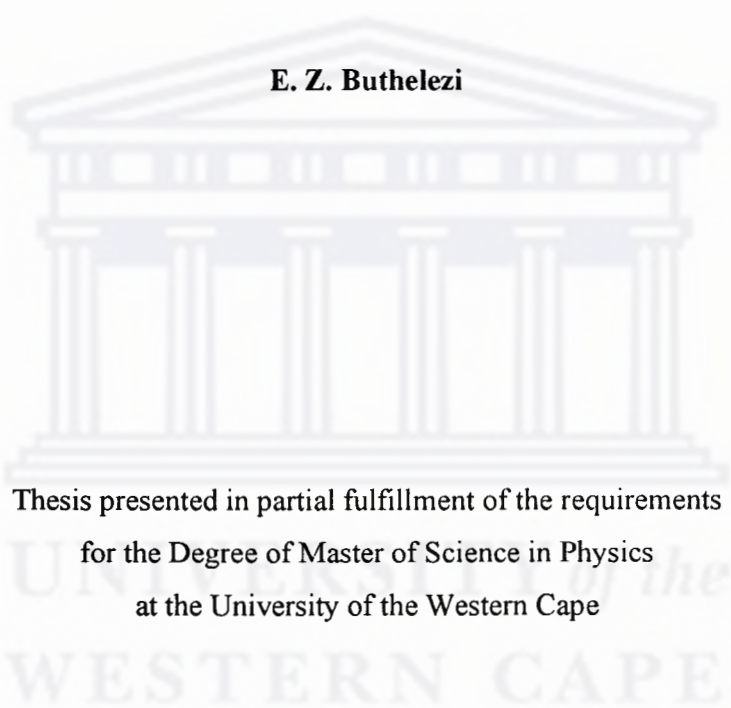


**THE DETERMINATION OF EXCITATION FUNCTIONS FOR $^{nat}\text{Rb}+p$ UP TO
100 MeV WITH AN EMPHASIS ON THE PRODUCTION OF ^{82}Sr**

by

E. Z. Buthelezi



Thesis presented in partial fulfillment of the requirements
for the Degree of Master of Science in Physics
at the University of the Western Cape

January 2000

Supervisor: Dr. A. Green
Co-supervisor: Dr. F. M. Nortier



Declaration

I, the undersigned, hereby declare that the work contained in this thesis is my own original work and has not previously in its entirety or in part been submitted at any university for a degree.

Signature: **Date:**

UNIVERSITY *of the*
WESTERN CAPE

The determination of excitation functions for $^{nat}\text{Rb}+p$ up to 100 MeV with an emphasis on the production of ^{82}Sr

Edith Zinhle Buthelezi

Submitted to the Department of Physics
January 2000, in partial fulfillment of the
Requirements for the degree of
Master of Science

Abstract

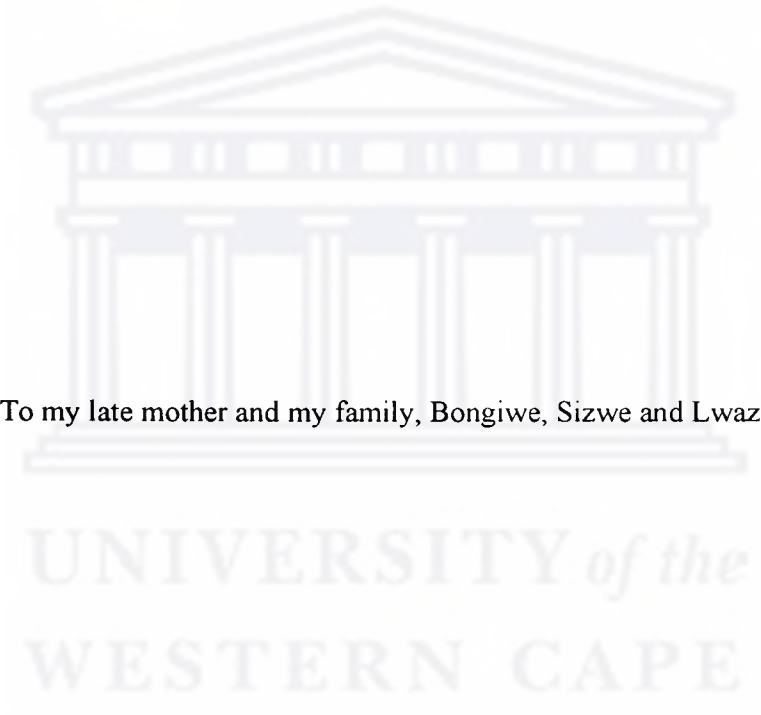
The radioisotope strontium-82 ($T_{1/2} = 25.55$ days) decays to short-lived ^{82g}Rb ($T_{1/2} = 76$ seconds) by 100% electron capture (EC). The short-lived ^{82g}Rb decays by 95.5% positron-emission β^+ and 4.5% EC to stable ^{82}Kr . Rubidium-82g is used in Positron Emission Tomography (PET) applications, including studies of myocardial infarction, kidney tissue and brain blood flow.

In the present study the excitation functions for the production of ^{82}Sr , other radio-strontiums and radio-contaminants produced in the proton bombardment of ^{nat}Rb were measured by means of the stacked-foil technique. Three stacks were prepared and were assembled from RbCl samples and aluminium- and copper- monitor foils. The RbCl samples were prepared by pressing the RbCl-salt into pellets having thicknesses of 200 mg/cm^2 for the energy region 40-100 MeV and 100 mg/cm^2 for the energy region below 40 MeV. The stacks were bombarded at the National Accelerator Centre cyclotron facility with beams having proton energies of 100.9 MeV, 66.8 MeV and 40.4 MeV and a nominal beam intensity of 100 nA.

After bombardment, the induced activity of the radioactive products in each target pellet and monitor foil were measured by means of γ -ray spectroscopy. For this purpose a calibrated HP-Ge detector coupled to a SILENA 16-k multi-channel analyzer was used.

The measured excitation functions for the relevant radioisotopes are presented and, where applicable, compared with previously published data. In some cases no other data were available in the literature for comparison purposes. Theoretical calculations using the computer code ALICE-IPPE were also done and were compared with the present data.

These excitation functions are used to suggest a suitable energy window for the production of a high quality ^{82}Sr product.

The logo of the University of the Western Cape is centered on the page. It features a stylized illustration of a classical building with a pediment and six columns. Below the illustration, the text "UNIVERSITY of the WESTERN CAPE" is displayed in a serif font, with "of the" in italics.

To my late mother and my family, Bongiwe, Sizwe and Lwazi

ACKNOWLEDGEMENTS

I wish to express my gratitude to all the people who contributed in one way or another to the completion of this thesis.

First of all, I would like to thank the Lord Almighty for all He has done for me during this period. Without Him none of this would have happened and for that I am in debt to Him. I thank Him for the patience; the strength and wisdom He has given the people who assisted in putting this work together.

My deepest thanks go to Dr. F. M. Nortier for his continual patience, advice and guidance. His door was always open to assist in every way he could. The enthusiasm he showed is appreciated. His professionalism has been inspirational.

I am particularly thankful to my co-promotor, Dr. A. Green for his guidance and support to date. He has been a great teacher all the way.

Thanks to my colleagues, Dawid de Villiers and Ian Schroeder. Dawid, you have been a great motivator during this period. Your sense of humour made everything much easier at times. Ian, thanks for the sleepless nights you spend with us. Your help was valuable and welcome at all times. To Johan Hanekom, thanks for the work you put in during the irradiations and for all the help you gave during target preparation.

Lastly, I would like to thank my family and all my friends for their support and understanding, especially, when I needed you. Keep it up and may God bless your dear hearts.

CONTENTS

CHAPTER 1: MOTIVATION AND OUTLINE OF THESIS	1
1.1 Introduction and motivation	1
1.2 Thesis Outline	4
CHAPTER 2: PASSAGE OF HIGH-ENERGY PROTONS THROUGH MATTER	5
2.1 Beam effects	5
2.1.1 Stopping power and energy loss	6
2.1.2 Path-length and range	7
2.1.3 Energy and range straggling	8
2.1.4 Small-angle multiple scattering	8
2.2 Nuclear reactions	9
2.2.1 Types of nuclear reactions	9
2.2.2 Reaction threshold	11
2.2.3 Cross-sections	12
2.2.4 Excitation functions	13
2.2.5 Reaction channels	13
2.3 Importance of nuclear data	14
CHAPTER 3: EXCITATION FUNCTION MEASUREMENTS	15
3.1 Introduction	15
3.2 Experimental aspects	15
3.2.1 Target stacks and irradiation	15
3.2.2 Monitor reactions	17
3.2.3 γ -Ray spectrometry	18
3.2.4 Data analysis	22
3.2.5 Cross-sections and uncertainties	25

CHAPTER 4: RESULTS AND DISCUSSION	27
4.1 Strontium-82	27
4.1.1 Excitation function	27
4.1.2 Calculated yields based on the excitation function	29
4.1.3 Production tests at high beam currents	29
4.2 Other strontium radioisotopes	32
4.3 Rubidium radioisotopes	35
4.4 Bromine and krypton radioisotopes	41
4.5 Comparison with theoretical calculations by means of ALICE-IPPE	43
CHAPTER 5: CONCLUSION	44
APPENDICES	
A1 Schematic illustrations of the tools for pressing and sealing of tablets	49
A2 Calculation of stopping powers	51
A3 Calculation of reaction Q-values	53
A4 Calculation of cross-section measurements and production yield	54
A5 Important parameters used in the ALICE-IPPE code	59
A6 Tables of measured cross-sections and production rates	61
REFERENCES	67

LIST OF FIGURES

2.1	Stopping power for protons in RbCl and Rb target materials	7
2.2	Representation of the path-length and the range of the proton beam inside a target material	8
3.1	Schematic illustration of the stack assembly	16
3.2	Schematic diagram of the experimental set-up used for the irradiation of the foil stack	17
3.3	Excitation function for $^{nat}\text{Al}(p,x)^{22}\text{Na}$	19
3.4	Excitation functions for the production of $^{62,65}\text{Zn}$ in $^{nat}\text{Cu}+p$	20
3.5	Schematic representation of the γ -ray spectroscopy set-up	21
3.6	Representation of the spectra used in the stripping approach	24
3.7	Representation of the superimposed RbCl and ^{22}Na spectra used in stripping	25
4.1	Experimental excitation function for the production of ^{82}Sr via the (p,xn) reaction on ^{nat}Rb	28
4.2	Calculated yields based on the measured excitation function for the production of ^{82}Sr	30
4.3	Schematic representation of the target arrangement for the production of ^{82}Sr at high currents	31
4.4	Excitation functions for the production of $^{81,83}\text{Sr}$ via the (p,xn) reaction on ^{nat}Rb	33
4.5	Excitation functions for the production of $^{80,85}\text{Sr}$ via the (p,xn) reactions on ^{nat}Rb	34
4.6	Excitation functions for the production of $^{81,81m}\text{Rb}$ in $^{nat}\text{Rb}+p$	37
4.7	Excitation functions for the production of $^{82,83}\text{Rb}$ in $^{nat}\text{Rb}+p$	38
4.8	Excitation functions for the production of $^{84,84m}\text{Rb}$ in $^{nat}\text{Rb}+p$	39
4.9	Excitation functions for the production of $^{79,86}\text{Rb}$ in $^{nat}\text{Rb}+p$	40
4.10	Excitation functions for the production of $^{77,80m}\text{Br}$ and ^{79}Kr in $^{nat}\text{Rb}+p$	42
5.1	Excitation functions for strontium isotope	45
A1.1	Schematic diagram of the punch-and-die set used for pressing tablets at the NAC	49
A1.2	Schematic representation of the cold-pressure-welding tool	49
A1.3	A thick RbCl target pellet prepared at the NAC for the ^{82}Sr production is sealed in the aluminium capsule	50

LIST OF TABLES

3.1	Counting sessions for each foil stack	22
3.2	Radioisotopes identified for the $^{nat}\text{Rb}+p$ nuclear reactions	23
4.1	Yield calculated for the production of ^{82}Sr in $^{nat}\text{Rb}+p$	29
4.2	Production yield of ^{82}Sr measured at EOB in production runs	32
5.1	Activities of radioisotopes at different times after EOB as observed in the irradiation of ^{nat}Rb	46
A5.1	Input parameters for the code ALICE-IPPE and values used	59
A6.1	Approximate cross-sections for ^{22}Na and $^{62,65}\text{Zn}$	61
A6.2	Cross-sections measured for the production of ^{82}Sr and its main radio-contaminants	62
A6.3	Cross-sections measured for the production of Rb isotopes in $^{nat}\text{Rb}+p$	63
A6.4	Cross-sections measured for the production of Br and Kr isotopes in $^{nat}\text{Rb}+p$	64
A6.5	Calculated thin target yield for ^{82}Sr based on the excitation function	65
A6.6	Calculated thick target yield for ^{82}Sr based on the excitation function	66

CHAPTER 1

MOTIVATION AND OUTLINE OF THESIS

1.1 Introduction and motivation

Proton accelerators are widely used to produce medically useful radioisotopes. Medical radioisotopes can be produced either by accelerators or by reactors. Radioisotopes produced in this way have properties that make them attractive as diagnostic tools in nuclear medicine.

Accelerator-produced radioisotopes have an advantage over reactor-produced ones because they are usually of a different element than that of the target. This makes chemical separation possible so that a very high specific activity can be achieved. Furthermore, most accelerator-produced isotopes are neutron deficient and usually decay by *positron emission* (β^+) or *electron capture* (ϵ), which makes them suitable for applications in diagnostic medicine. Radioisotopes emitting β^+ particles are very useful when combined with three-dimensional imaging techniques such as *Positron Emission Tomography* (PET) which is employed in diagnostic studies. In the case of radioisotopes which decay by electron capture, the absence of particle emission is an advantage in that it helps to reduce the radiation dose received by the patients.

In order to develop cyclotron-based production methods for medical radioisotopes one needs to acquire accurate knowledge of the relevant nuclear cross-section data. From accurately determined excitation functions one can then derive the optimum production rates and make decisions on how to achieve them.

In South Africa, the National Accelerator Centre (NAC) provides the medical community, as well as other multi-disciplinary scientific communities, with a large variety of charged particle beams generated by a cyclotron. A 66 MeV proton-beam is utilized for the routine production of radioisotopes. Different medically useful radioisotopes are produced at NAC and supplied to hospitals and clinics. Introducing new isotopes to the system expands the list.

Amongst the accelerator-produced radioisotopes, strontium-82 (^{82}Sr) enjoys wide usage in nuclear medicine. Strontium-82 with a half-life of 25.5 days decays by 100% electron capture (EC) to the ground state of rubidium-82 (^{82g}Rb) but does not decay to ^{82m}Rb . The ground state ^{82}Rb has a half-life of 76 seconds and it decays by 95.5% positron emission (β^+) and 4.5% EC to stable krypton-82 (^{82}Kr). ^{82g}Rb emits only one gamma ray (γ -ray) with an abundance of more than 1% present in its decay. This γ -ray has an energy of 776.5 keV and its absolute abundance is 13.4%. Because ^{82g}Rb emits β^+ , it provides a high flux of positrons for annihilation. Due to its short half-life, this radioisotope allows one to examine patients without subjecting them to large radiation doses. ^{82g}Rb is extensively used in clinical medicine as a diagnostic tool in PET studies. In practice, ^{82g}Rb is obtained from ^{82}Sr - ^{82}Rb generator systems by eluting it with a solvent. The eluted ^{82g}Rb is then injected to a patient. ^{82g}Rb can be used in different diagnostic studies such as myocardial infarction (disorder of the heart muscle), kidney tissue and brain blood flow.

Presently, ^{82}Sr is mainly produced via the $^{nat}\text{Rb}+p$ route in the proton energy region of 30-60 MeV, [Dep90, Hor80, and Lag93] and via a spallation process on molybdenum, $^{nat}\text{Mo}(p,\text{spall})^{82}\text{Sr}$ with an 800 MeV proton beam [Bey89].

Several papers have been published on the production of ^{82}Sr by the proton bombardment of rubidium targets by means of a stacked-foil method. Most of these publications discuss the production routes which are commonly used worldwide. These routes involve the use of either the natural rubidium (^{nat}Rb) targets [Dep90, Lag93] or the enriched rubidium (^{85}Rb) targets [Hor80]. In the case of Deptula *et al.* [Dep90], thin ^{nat}Rb targets were bombarded with a 100 MeV proton beam of intensity 2.8 μA . The reported thick target yield was 0.43 $\text{mCi}\cdot\mu\text{A}^{-1}\text{h}^{-1}$. Whereas, in the case of Lagunas-Solar [Lag93] thin ^{nat}Rb targets were bombarded with a 70 MeV proton beam (no intensity reported). In his previous publication [Lag92] he reported that in his unpublished results a yield of 0.35 $\text{mCi}\cdot\mu\text{A}^{-1}\text{h}^{-1}$ for a 42 MeV exit window was achieved. Horiguchi *et al.* [Hor80], bombarded enriched ^{85}Rb targets with a 70 MeV proton beam of intensity 0.5 – 1 μA and reported a yield of $\sim 0.47 \text{ mCi}\cdot\mu\text{A}^{-1}\text{h}^{-1}$.

In the spallation method a thick molybdenum target is bombarded with protons (800 MeV) at currents up to 500 μA . Bombardment times normally vary from two days to one month. After

bombardment the relevant radioactive product is separated from its radio-contaminants using complicated chemical procedures. The product is then γ -ray spectroscopically measured and the activity determined. Yields of ~ 61 - $100 \mu\text{Ci} \cdot \mu\text{A}^{-1}\text{h}^{-1}$ have been reported [Ver93].

According to Mausner *et al.* [Mau87] the spallation reaction on ^{nat}Mo is inferior in radionuclidic purity compared to the $^{nat}\text{Rb}+p$ reaction. This is mainly due to the fact that it is impossible to clear ^{82}Sr of the associated long-lived ^{85}Sr ($T_{1/2} = 64.9$ days), ^{89}Sr ($T_{1/2} = 50.5$ days) and ^{90}Sr ($T_{1/2} = 28.5$ years). Since the production of ^{82}Sr via ^{nat}Rb does not involve the $^{89,90}\text{Sr}$ impurities and the high yields achieved ($\sim 0.43 \text{ mCi} \cdot \mu\text{A}^{-1}\text{h}^{-1}$) [Dep90] make this route a much more attractive way of producing ^{82}Sr . Despite the usefulness of ^{82}Sr in diagnostic medicine, the task of producing it still remains fairly complicated and, since some amounts of impurities are inevitable in both production reactions, a continued demand for this radioisotope has encouraged on-going development and refinement of its production.

The bombardment of rubidium targets with protons in the 30-70 MeV energy range has been reported as a better method than those two discussed above, because it gives high yields and low level radioisotopic impurities [Ver93]. At the NAC the radioisotope team is planning on producing ^{82}Sr via this method. The present work is dedicated to the investigation of this production route through the study of the experimental excitation functions for the production of ^{82}Sr and its radio-contaminants $^{80,81,83,85}\text{Sr}$ by means of the stacked-foil technique. Three stacks were prepared (100 MeV, 66 MeV and 40 MeV) where the first stack covered the 60-100 MeV proton energy region, the second stack covered the 30-66 MeV proton energy region and the last stack covered the low energy region from threshold up to 40 MeV. These stacks were bombarded with proton beams of low intensities (100 nA). The measured excitation functions were then compared with the theoretical calculations and with previously published data.

In addition in this work, excitation functions for the production of other radioisotopes in the proton bombardment of ^{nat}Rb have also been measured. These are $^{79,81,82m,83,84,86}\text{Rb}$, $^{77,80m}\text{Br}$ and ^{79}Kr . The results for these important radioisotopes are also included in this work and contribute to the expansion of the existing worldwide excitation function database. The need for such data has been stressed previously [Dep90, Hor80 and Lag93].

1.2 Thesis outline

The thesis is structured as follows:

- The important physical processes relevant to the production of radioisotopes and the stacked foil technique are discussed in Chapter 2. These processes include the effects of the beam on the target material and nuclear reactions. The discussion on the importance of excitation function data is also covered. Beam effects include the stopping power and energy loss of protons in the target material, energy, path-length and range straggling and multiple scattering. In the “nuclear reactions” section I discuss reaction threshold, cross-sections, excitation functions and reaction channels.
- Chapter 3 is a detailed discussion of the techniques involved in the measurement of excitation function for the production of ^{82}Sr by means of the stacked-foil technique. The discussion includes the experimental details such as the preparation of the stack and irradiation details, quantitative γ -ray spectroscopic analysis, the measured cross-sections and their uncertainties.
- Measured excitation functions of all the radioisotopes for which cross-sections could be measured and production rates calculated from the ^{82}Sr excitation function are given and discussed in Chapter 4. The excitation functions presented are also compared with theoretical calculations and with previously published data. A brief discussion on the production of ^{82}Sr at high beam currents is also included. The chapter closes with the presentation of some theoretical calculations using the ALICE-IPPE code.
- Chapter 5 presents the general conclusions as well as suggestions for future developments.

CHAPTER 2

PASSAGE OF HIGH-ENERGY PROTONS THROUGH MATTER

During bombardment of a target with a beam of protons, collisions occur between the beam of particles and nuclei of the target. There are different kinds of interactions, some of which are important for the production of a particular radioisotope. This chapter discusses some of those physical processes that are generally thought to be the most important in radioisotope production and in the application of the stacked-foil technique.

2.1 Beam effects

When charged particles like protons travel through matter they interact with the atomic electrons via the Coulomb interaction. On passage through the target they lose their energy by interacting with many such electrons. The impulse exerted on an atomic electron when a proton passes in its vicinity might be sufficient either to raise the electron to a higher excitation level within the atom or, in some cases remove it completely from the atom (ionization). Another possibility is that the proton can be involved in a single electron collision in which case a δ -ray (secondary electron) may be emitted.

The kinetic energy lost to a single electron is small compared to the total energy of the proton. However, since the proton interacts with many electrons, its velocity decreases continuously until it is stopped. The track the proton follows is roughly straight because the angle of deflection of the proton from any such encounter is negligibly small due to the large difference in mass of an electron and the proton.

The energy loss process is usually described in terms of a few quantities. The most commonly used ones are introduced and described below.

2.1.1 Stopping power and energy loss

The stopping power $S = - \frac{dE}{dx}$ is defined as the linear rate at which a charged particle loses its energy when passing through matter. This quantity is also frequently referred to as the “rate of change of energy” and is expressed as a function of kinetic energy, the charge and the mass of the projectile. It has units of MeV/(g.cm⁻²) or MeV/cm (see Appendix A2 for the calculation of the stopping power for protons). Since the number of interactions per unit length is very large, a substantial cumulative energy loss occurs in relatively thin layers of the target material. In practice two main processes contribute to the stopping power for protons in a target material: *nuclear stopping and electronic stopping*.

At high energies when the proton interacts with the atomic electrons in the target its own velocity is usually much higher than the velocities of the electrons. The proton then loses energy chiefly through electronic excitation and ionization of the target atoms. The energy loss as a result of both these processes is defined as *electronic stopping*. It essentially occurs at relatively high proton velocities. At some stage the proton’s velocity is reduced to a point at which it becomes comparable with the velocity of the K-shell electrons. When this happens the proton may pick up an electron at which point the stopping power drops off towards the end of its trajectory and it may pick up electrons and lose them many times until it finally stops.

At these low energies where the velocity of the proton is much smaller than the velocity of the atomic electrons, electron stopping is no longer dominant but the interaction with the relatively small nuclei of the target atoms starts to play a role. If the proton comes into close contact with the nucleus, an elastic nuclear collision may occur. The kinetic energy of the proton is transferred to the nucleus setting it in motion as a whole. The proton loses kinetic energy so as to satisfy conservation of energy and momentum for the interaction. Since the mass of the target nucleus is larger than that of the proton, the energy lost to the atomic nucleus is very little. This energy loss process is called *nuclear stopping*.

Figure 2.1 shows the stopping power as a function of energy for protons in RbCl and Rb targets. All the stopping power values in this study were calculated using the expressions of

Anderson and Ziegler [And77]. In this work the stopping power was calculated in order to determine the energy in the stacks.

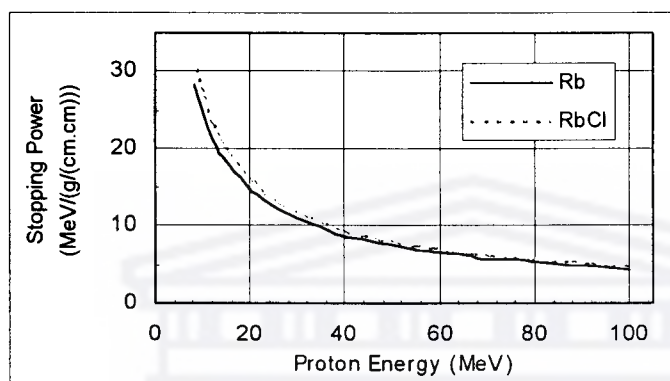


Figure 2.1: Stopping power for protons in RbCl and Rb target materials

2.1.2 Path-length and range

Path-length is defined as the average distance covered by a beam of protons travelling from the point where it enters the material with a specific kinetic energy to the point at which the kinetic energy is equal to zero. It includes the track deflections caused by angular scattering. The range of the beam of energetic protons in a target is defined as the mean depth of penetration measured along a *straight* line parallel to the original direction of the motion of the protons. The relation of range to energy loss is given by:

$$R = \int_0^R dx = \int_0^{E_p} \frac{dE}{\left(\frac{dE}{dx}\right)},$$

where $(-dE/dx)$ is the stopping power for protons in a target material. As illustrated in Figure 2.2, the range is always less than the path-length due to angular deflection caused by multiple scattering from atomic nuclei (see section 2.1.4). The range becomes increasingly important in the low energy region (40 MeV stack) where the energy-loss is much higher.

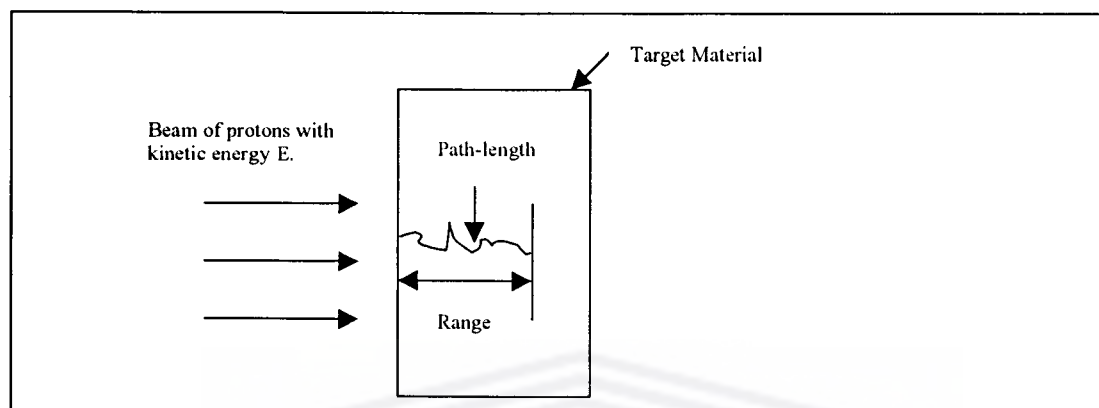


Figure 2.2: Representation of the path-length and the range of the proton beam inside a target material.

2.1.3 Energy and range straggling

The energy lost by a proton in a collision with an atomic electron is not always the same since the impact parameter (distance of closest approach) is not predictable and varies considerably. The number of collisions per unit length also varies for individual incoming protons. Hence, the energy lost per unit distance traveled is not constant and so two protons with the same energy need not come to a stop at the same range or have the same path-length. This variation is known as *straggling* and has a statistical nature. At low-energies when fluctuations in the effective charge of the proton also occur, the fluctuations in the fractional energy loss per collision become larger, especially at energies where nuclear stopping is dominant. Through nuclear stopping the proton will then undergo scattering. Thus mono-energetic beams of protons do not have a unique range in the target material. The beam will acquire an energy spread after passing through a thickness of target material. This spread increases with increasing depth of penetration. In short, range straggling results from energy straggling.

2.1.4 Small-angle multiple scattering

Multiple scattering of charged particles is caused by deflections of protons by the atomic nuclei. A single proton undergoes many such small angle deflections. Hence, when a beam of

mono-energetic protons traverses a target an increasing angular spread in the beam with increasing thickness is observed and the beam broadens at the end of the stack. Multiple scattering, energy and range straggling are all considered in the designing of the stack.

2.2 Nuclear reactions

As a proton travels through matter it is possible that it interacts with a target nucleus. If the proton does not come into close contact with the nucleus of the target atom, nuclear elastic scattering takes place in which a part of the proton's kinetic energy is transferred to the nucleus, setting the nucleus into motion. This process is called *elastic nuclear scattering*. However, at close encounters there may be some internal disturbance caused in the nucleus placing the target nucleus in an excited state. This process is known as *inelastic nuclear scattering*.

At even closer encounters the proton can penetrate the target nucleus and be absorbed bringing the nucleus into a highly excited state. De-excitation follows immediately and it can occur in two different ways. Firstly, several γ -rays may carry away the excitation energy with the result that the proton is captured and a new (sometimes a radioactive) nucleus is formed. Secondly, the excitation energy of the nucleus may be concentrated in one or more of its nucleons, which can then leave the nucleus. Both alternatives are called *nuclear reactions*. One of these three types of nuclear reactions can occur: direct reactions, compound nucleus reactions and pre-equilibrium reactions.

2.2.1 Types of nuclear reactions

A direct reaction takes place when the incident particle interacts with only a few nucleons in the target nucleus, some of which may be directly ejected. In this case the majority of nucleons are not disturbed. There is a strong possibility that the incoming particle will leave the target nucleus again after losing some of its kinetic energy during these few collisions. This reaction takes place very fast (10^{-22} seconds), before the nucleus progresses to an intermediate excited compound state. This type of reaction contributes in the excitation function at high incident energies.

A compound nucleus is formed when the incoming charged particle and the target nucleus merge for a complete sharing of energy before any nucleons are ejected. The identity of the incoming nucleon is lost. This excited state is referred to as a “quasi-stationary” state because the excitation energy makes the nucleus unstable with respect to the emission of particles. The nucleons in the compound nucleus exchange energy with each other through many collisions. Due to statistical fluctuations in energy a concentration of energy will occur allowing a single nucleon to escape. If the original excitation energy of the compound nucleus is great enough there might be sequential emission of several particles from the excited compound nucleus. Each of these emitted particles would have relatively low kinetic energy. In summary, the compound nucleus mechanism occurs in two stages. Firstly, the incident particle is captured with the random sharing of energy among the nucleons in the compound nucleus. Secondly, there is the evaporation of particles from the excited compound nucleus. The half-life of this reaction ranges from 10^{-18} to 10^{-16} , seconds, considerable longer than for direct reactions.

The two mechanisms discussed above describe the extremes of a nuclear reaction which may occur in the interaction of an incident proton with a target nucleus. However, there are some phenomena that cannot be explained by either of these mechanisms. At high energies it is possible for particle emission to take place after direct ejection has occurred, but long before the equilibrium of the compound nucleus is attained. This implies that the pre-equilibrium reactions occur between 10^{-22} and 10^{-16} seconds. Pre-equilibrium or pre-compound reactions account for this intermediate emission between the fast direct reaction and slow compound nucleus reaction. This mechanism is evidenced in the excitation functions of the proton-induced nuclear reactions where the cross-section tail falls steadily with increasing proton energy.

The above discussion acknowledges the possible nuclear reactions that can take place when a proton interacts with a target material. Nuclear reactions are usually characterized by certain physical observables. These observables include reaction threshold, reaction cross-section, and excitation function (the relation of the reaction cross-section to incident proton energy).

2.2.2 Reaction threshold

Conservation of energy and momentum determine the minimum energy required for a reaction. This energy is known as the “Q-value” of the reaction. The Q-value balances the masses before and after the reaction. If $Q > 0$ then energy is liberated from the system; if $Q < 0$ then energy must be supplied to the system by the incident particle for the reaction to occur. The Q-value is expressed as

$$Q = (m_{\text{initial}} - m_{\text{final}}) c^2$$

where m_{initial} and m_{final} are the masses of the reactants and products respectively and c is the speed of light. The calculations of the Q-values for the proton-induced nuclear reactions obtained in this work are found in Appendix A3. The threshold energy T_{th} is defined as the absolute minimum kinetic energy value below which a reaction is not possible. It is given by

$$T_{\text{th}} = (-Q) \frac{m_1 + m_2}{m_2}$$

where m_1 and m_2 are the masses of the incident particle and target nucleus respectively. The masses come from the center-of-mass system where the relevant mass of the reacting particles is given by the reduced mass ($\mu = (m_1 + m_2)/m_2$). This threshold condition is only valid for $Q < 0$. If $Q > 0$, then the threshold condition does not exist since the reaction needs no help. The Coulomb barrier provides another threshold condition. For the nuclear reaction to occur, the nucleons must touch. This means that the Coulomb potential barrier around the target nucleus must be overcome. This barrier is caused by the repulsion between the positive charges of both the incident particle and the target nucleus. It is expressed as

$$V_C = \frac{z_1 z_2 e^2}{r_1 + r_2},$$

Where r_1 and r_2 are the nuclear radii of the particle and the target nucleus, respectively, and $z_1 e$ and $z_2 e$ are the charges of the incoming particle and the target nucleus.

2.2.3 Cross-sections

The cross-section (σ) is defined as the measure of probability for the interaction of a particle with a target system. This observable has the dimensions of a surface area and is expressed in mbarn ($1 \text{ cm}^2 = 10^{27} \text{ mbarn}$). For a beam of particles striking a thin target with thickness Δx , that is, a target in which the beam is attenuated only infinitesimally, the cross-section for the production of a particular residual nucleus or radioisotope can be calculated from

$$R_i = I\sigma N_o$$

where R_i is the rate of production of the radioisotope- i , I is the number of incident particles per unit time (proton flux rate) and N_o is the number of target nuclei per unit area.

In the case of high-energy beams it is often possible to produce a specific radioisotope via different nuclear reactions since several nuclear reaction-channels may be available to form either a short-lived precursor or the particular radioisotope directly. Hence, two distinct reaction cross-sections can be defined. When a single stable isotope (or target element) undergoes different nuclear reactions to produce a particular radioisotope directly or via its precursors, the production cross-section for this radioisotope is usually called the *cumulative cross-section*. It is also possible that the target has more than one stable isotope, which may also undergo different nuclear reactions to obtain a particular radioisotope. The sum of the cross-sections $\sigma_i(E)$ for all possible nuclear reactions that contribute to the formation of that radioisotope is then called the *effective cross-section* $\sigma(E)$. In cases where the target material used has more than one isotope, only the effective cross-section is applicable.

The expressions for the calculation of cross-sections in this work are discussed in detail in Appendix A4. The calculated values obtained from measurements for the relevant radioisotopes and other by-product radioisotopes are found in Appendix A6.

2.2.4 Excitation functions

The curve showing how the cross-section of a nuclear reaction varies with the energy of the bombarding particle is called an *excitation function*. The shape of an excitation function can be determined by means of a stacked-foil measurement. This is done by exposing several target foils in a stack (with appropriate energy degradation between the foils) to the same beam. After irradiation, foils are counted and the spectra are recorded. A quantitative analysis of the γ -ray spectroscopy follows. The cross-sections are then determined for the production of specific radioisotopes.

Several radioisotopes are usually produced in a mono-isotopic target, especially at high-bombarding energies. This is due to the fact that more than one nuclear reaction is possible in a target. Also, in a target which consists of several stable isotopes, it is often possible to produce a specific radioisotope via different nuclear reactions and to produce several other radioisotopes. To develop a suitable production route for a medical radioisotope, it is therefore essential to know the excitation functions for the various possible routes. In addition to this, knowing the excitation functions for the other radioisotopes produced and also knowing which isotope will eventually end-up as radio-contaminants in the final product, are often crucial.

The excitation function measurements are discussed in chapter 3 and the results are presented in Chapter 4.

2.2.5 Reaction channels

The number of reaction channels depends on the energy of the beam. As one increases the beam energy, the number of possible reactions with the same target nucleus increases. High-energy beams thus offer a large variety of radioisotopes to be produced from the same target. Further, the fact that more than one radioisotope is produced in addition to the desired one poses a problem.

2.3 Importance of nuclear data

Cross-section data for the production of a specific radioisotope are needed to determine the optimum energy range of a production process. Optimum energy range refers to that energy which gives the maximum yield of the desired radioisotope and the minimum amount of impurities. The increased number of reaction channels at high energies means more nuclear data are required due to the broadening range of isotopic and non-isotopic impurities formed. Non-isotopic products can be removed by chemical separation whilst the isotopic products can only be checked and suppressed by proper selection of the incident particle and energy range in the target through accurate knowledge of relevant excitation function data.

In this work the excitation functions for the production of ^{82}Sr and of the other radioisotopes produced in the bombardment of natural rubidium with protons are presented and compared with published data.



UNIVERSITY of the
WESTERN CAPE

CHAPTER 3

EXCITATION FUNCTION MEASUREMENTS

3.1 Introduction

To develop a production process for a particular radioisotope one requires an understanding of relevant nuclear cross-sections. This can be achieved by measuring the excitation functions for the production of the relevant radioisotopes. Knowing the excitation function for the production of the primary radioisotope of interest enables one to estimate the yield of the radioisotope to be produced and to determine the optimum energy range for its production. Therefore, if the excitation functions for the primary radioisotope and for its radio-contaminants are known, the best bombardment conditions can be chosen to maximize production yield while keeping the impurities to a minimum. This can be accomplished by measuring cross-sections for the relevant nuclear reactions in thin targets at different incident particle energies.

In this experiment, the excitation functions for the production of strontium-82 and other by-product radioisotopes were measured by means of the stacked-foil technique. This technique has the advantage that it permits the measurement of a number of data points over a range of proton energies in a single irradiation. A stack of samples is irradiated and each sample is counted individually afterwards. The incident protons lose their energy when passing through the stack so that different energies are applicable to each sample, making it possible to measure cross-sections at several energies with a single irradiation.

3.2 Experimental aspects

3.2.1 Target stacks and irradiation

RbCl salt (purity > 99.9 %) obtained from E.Merck (Darmstadt, Germany) was used as a target material. The salt was dried under vacuum for forty-eight hours to remove moisture. Small quantities were weighed and transferred to a punch-and-die set for pressing (see Figure A1.1, Appendix A1 for a detailed view of the pressing tools). Vacuum was applied to the

assembled tool for two minutes using an Alcatel pump which is operated at the pressure of 15 bar (1500kPa). A uni-axial pressure of 2 tons/cm² was then applied to the salt for half a minute with the vacuum pump still active. In this way, the salt was pressed into a very thin disc-shaped pellet of 20-mm diameter. After breaking the vacuum, the RbCl pellet was removed from the pressing tool for inclusion in a foil stack. Three stacks were prepared for proton beam energies of 100.1 MeV, 66.8 MeV and 40.4 MeV. Pellets with a nominal thickness of 200 mg/cm² were pressed for the 100.1 and 66.8 MeV stacks and 100 mg/cm² for the 40.4 MeV stack. Each pellet was weighed and labeled.

Aluminum and copper monitor foils obtained from Goodfellows (Cambridge, UK) were placed downstream of each RbCl pellet in the stack. Copper was used as a monitor foil at low energies (~25 MeV). The aluminum (purity > 99.999% and thickness of 67.5 mg/cm²) and copper (purity > 99.9% and thickness of 111.5 mg/cm²) were cut into discs of 19-mm diameter, cleaned, weighed and labeled. The stack was assembled (see Figure 3.1) and mounted in an appropriate stack-holder. The stack-holder was then fitted onto a water-cooled flange and placed in the proton beam for irradiation (see Figure 3.2). The target remained dry during the irradiation period.

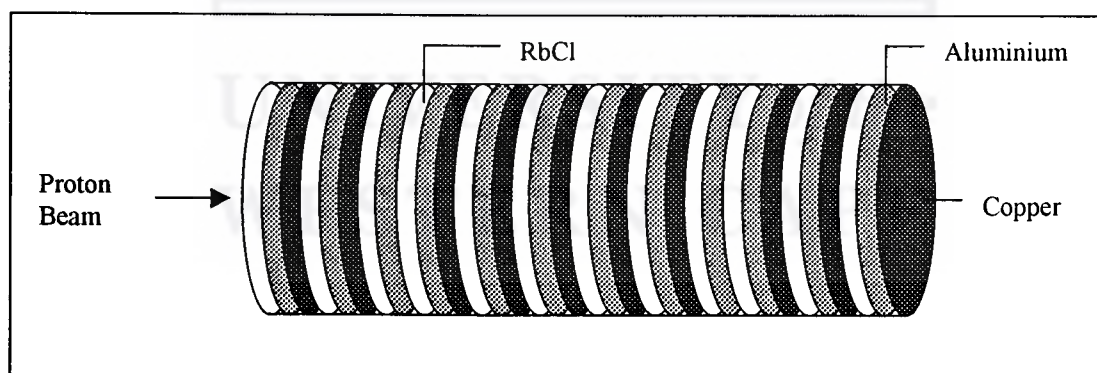


Figure 3.1: Schematic illustration of the stack assembly.

The beam was focused and aligned to strike the center of the target prior to irradiation by means of a BeO screen (250 μm thick) and a television camera (see Figure 3.2). To confirm the beam focus and position, autoradiograms (Polaroid instant film pictures) of some target pellets were taken at the end of their bombardment. In addition to this, a post-irradiation blue beam spot was clearly visible at the center of each RbCl pellet.

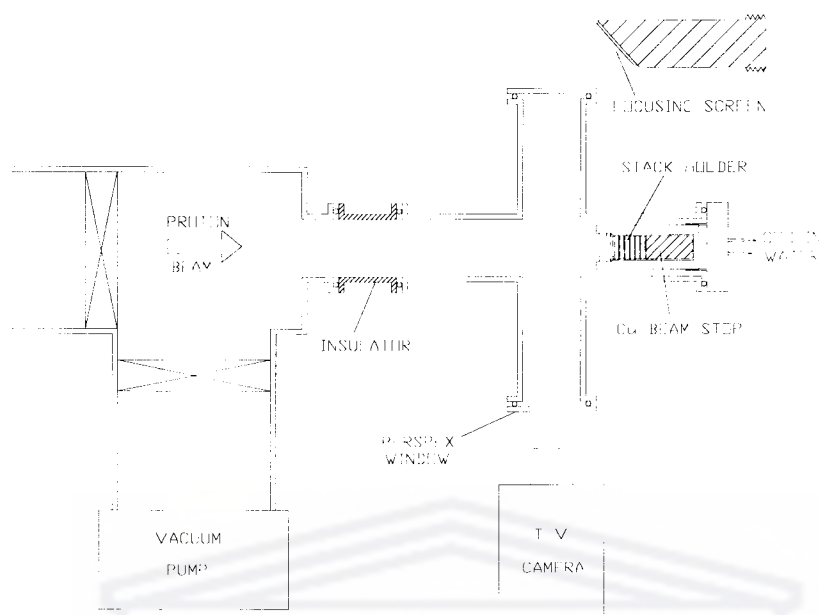


Figure 3.2: Schematic diagram of the experimental set-up used for the irradiation of the foil stack. For beam focusing purposes the BeO focusing screen replaces the stack-holder.

The stacks were irradiated with proton beams of 100.1 MeV, 66.8 MeV and 40.4 MeV primary energy, all with a nominal beam intensity of 100 nA. Beam intensity fluctuations were less than 5 % and were recorded for all energy-stacks. The bombardment time was one hour for each stack and in each case the protons were stopped directly behind the stack by a copper beam-stop.

3.2.2 Monitor reactions

Accurate cross-section values minimize the uncertainty in the excitation curve. One of the main factors that contribute to the uncertainty in experimental cross-sections is the estimated beam flux. The beam flux can be obtained by measuring the electric charge induced. This is achieved by mounting the target in front of a properly designed Faraday cup. However, if such an arrangement is not available, measurement of the proton flux may not be accurate. The use of monitor reactions is usually a more common means of measuring the proton flux because a much simpler target arrangement is required. A nuclear reaction of an accurately

known excitation function is chosen and monitor foils of an appropriate material are then included in the stack.

An approximate proton flux was measured by accumulating the charge with a Brookhaven Instrument Corporation 1000C current integrator while an accurately measured proton flux was eventually obtained from the well known excitation functions for the $^{nat}\text{Al}(p,X)^{22}\text{Na}$ and $^{nat}\text{Cu}(p,X)^{62,65}\text{Zn}$ reactions. The approximate cross-sections obtained from these measurements are listed in Table A6.1 in the appendix. Figure 3.3 shows a comparison between the approximate excitation function of $^{nat}\text{Al}(p,X)^{22}\text{Na}$ obtained in this work and the data presented by Steyn *et al.* [Ste90]. From the figure it is clear that there is an excellent agreement between the data points in the energy range 40-100 MeV. Hence, the approximate cross-section data for the 66 MeV and 100 MeV stacks obtained from this work was multiplied by a factor of one.

In the low-energy region (40 MeV stack) the excitation functions of $^{nat}\text{Cu}(p,X)^{62,65}\text{Zn}$ were used as monitor reactions. The approximate cross-section measurement data are listed in Table A6.1 in the appendix and are compared in Figure 3.4 with the data presented by Mills *et al.* [Mil92]. The approximate cross-sections measured in this work are higher than those of Mills *et al.* but they are within the error of the data presented by Mills *et al.* This implied that the secondary electrons (at least 99% of them) did not escape from the stack and therefore, the approximate cross-section data obtained in this work were only multiplied by a factor of one. Hence, the approximate proton flux was taken as the accurate value.

3.2.3 γ -Ray spectrometry

After irradiation, the γ -rays of the radioactivity induced in each target pellet and monitor foil were counted with accurately calibrated HPGe (High Purity Germanium) detectors, coupled to a SILENA 16k multi-channel analyzer system, (see Figure 3.5). The detector is mounted at

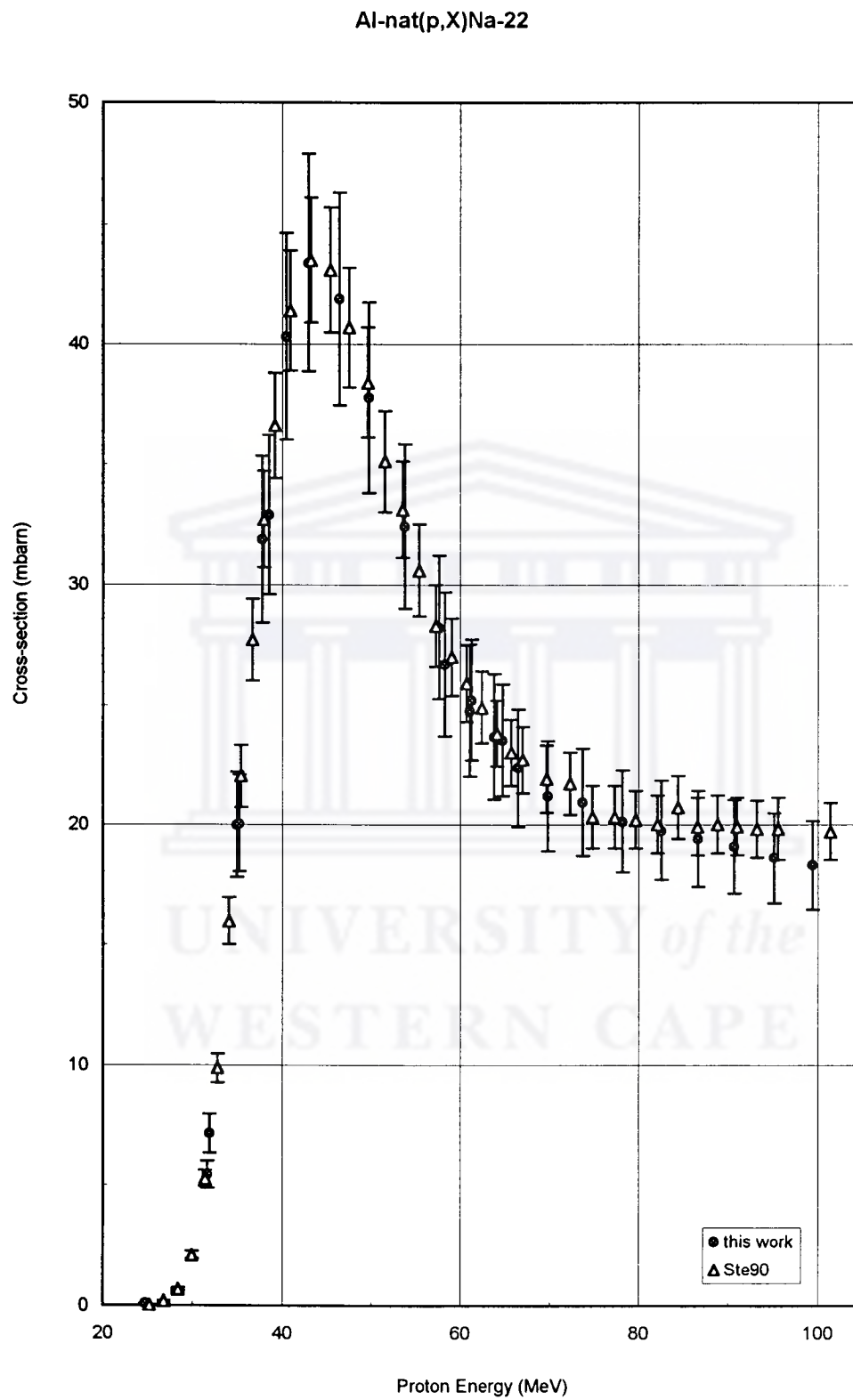
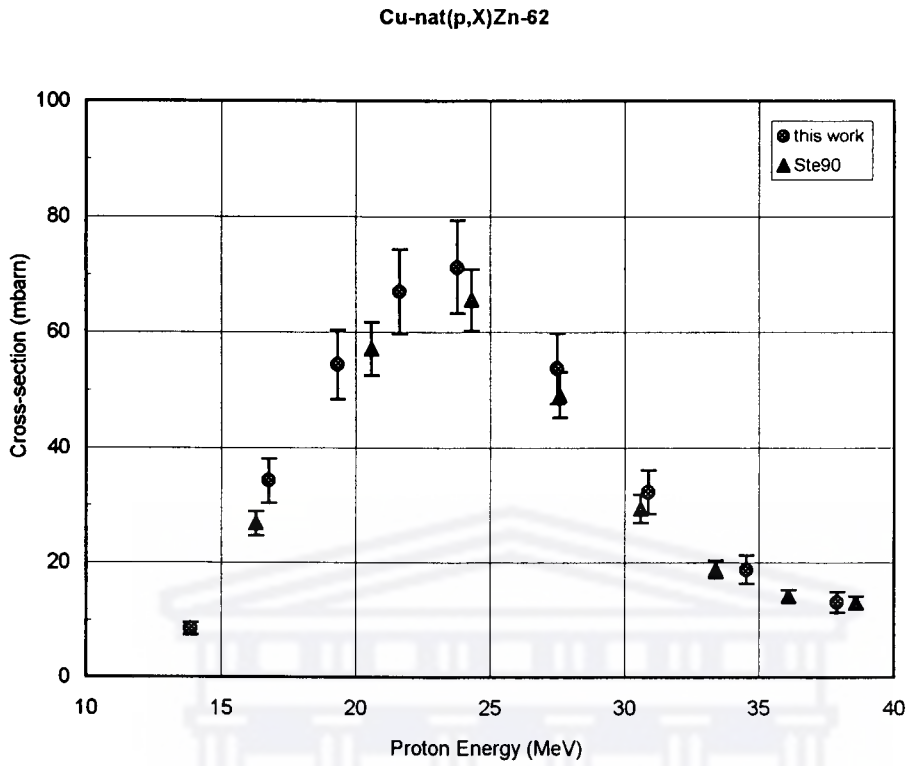
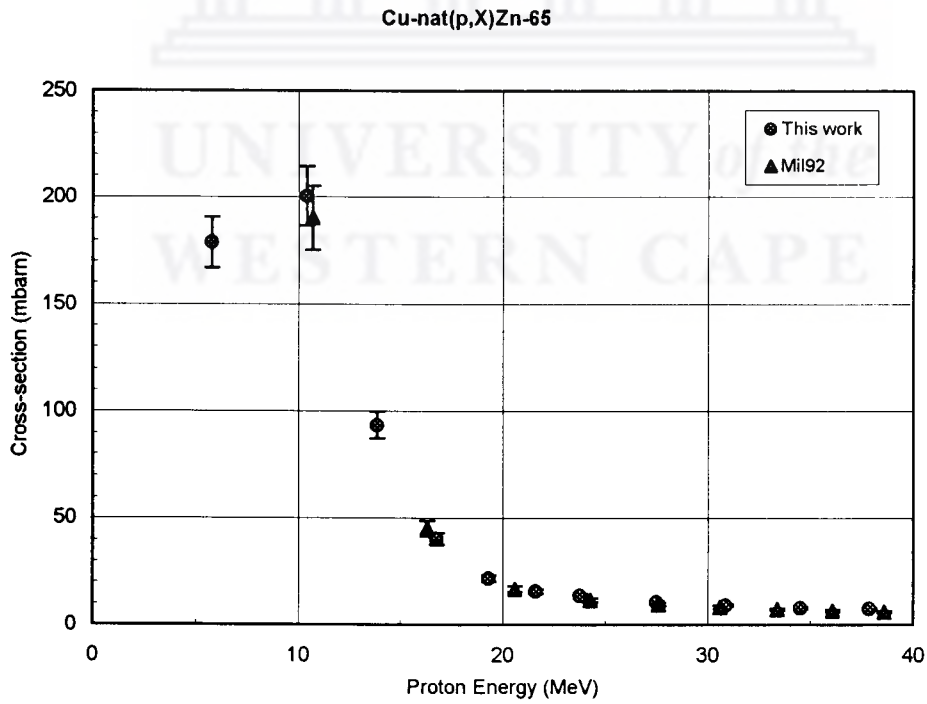


Figure 3.3: Excitation function of Na-22. The approximate data obtained in this work are compared with the published data of [Ste90].



(a)



(b)

Figure 3.4 (a,b) Excitation functions for the production of Zn-62, 65 from Cu-nat+p. approximate data from this work are compared with the data from [Ste90] and [Mil92]

the end of a 2-meter long bench with a movable holder. The set-up enables the setting of source-to-detector distances with a high degree of repeatability. The multi-channel analyzer (MCA) system has 16384 channels of which 4196 were used for a single spectrum. It also incorporates a 700 MHz ADC (Analogue to Digital Converter) and a Silena Model 7614 spectroscopy amplifier, which includes electronic circuitry for the rejection of pile-up pulses and a live-time correction.

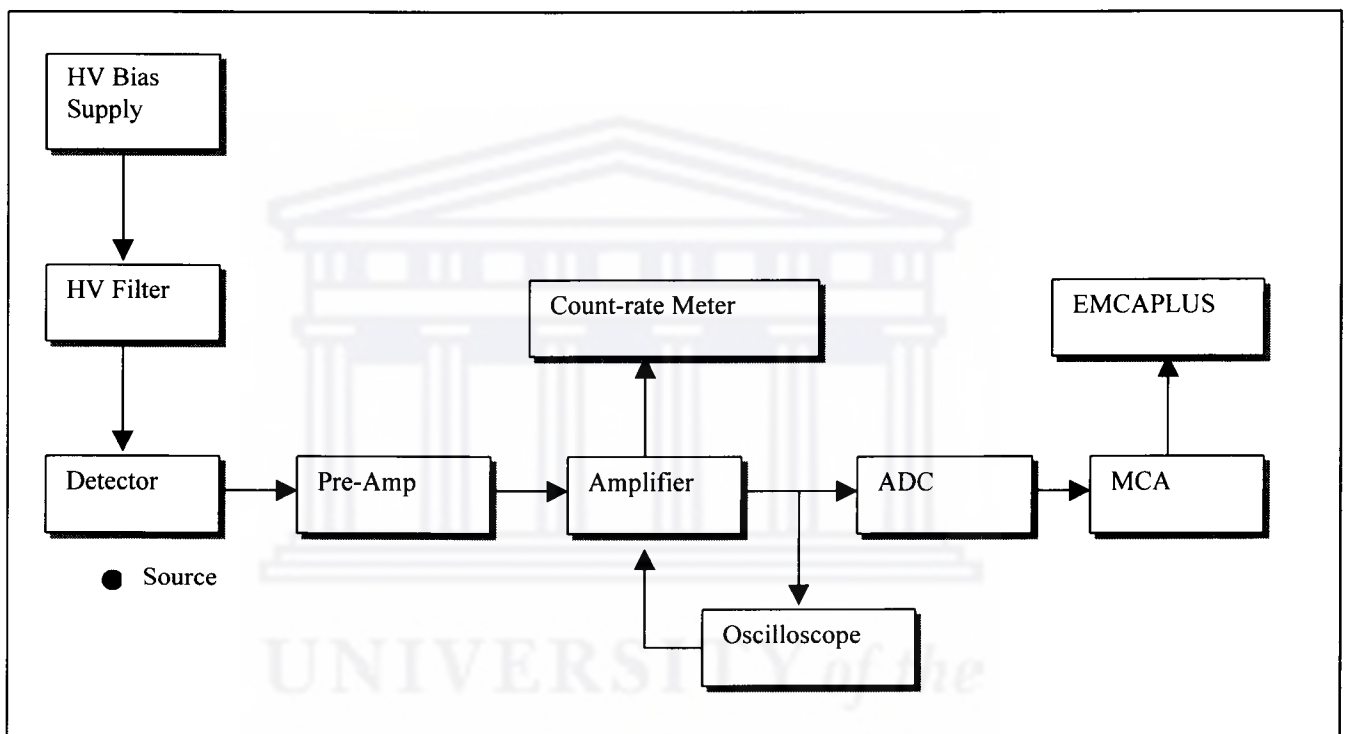


Figure 3.5: Schematic representation of the γ -ray spectroscopy set-up.

Two different detectors were used: (a) ORTEC HPGe detector (with Be window) which has a resolution of 2.14 keV full width at half-maximum (FWHM) at 1408 keV and (b) a HPGe-DSG detector (Detector Systems GMBH) with FWHM of 1.82 keV at 133 keV and 1.92 keV at 1408 keV. The detector efficiencies at various γ -energies and counting geometries were determined from the relevant γ -ray peaks of ^{152}Eu , ^{133}Ba and ^{241}Am sources supplied by Amersham Plc, UK. The energy calibration (calibration of channel number in terms of energy) is done prior to the start of the counting sessions. This was accomplished by using the spectra of ^{241}Am (13.9 - 59.5 keV), ^{133}Ba (80.9 - 383.9 keV) and ^{152}Eu (121.78 - 1408.03

keV) sources because they have several peaks with accurately known energies spread across the entire γ -energy region of interest (13 – 1420 keV).

Corrections for decay losses during and after irradiation were made (Section A4.2, Appendix A4). Counting was done in sessions according to the expected radioisotope half-lives. For the measurement of the short-lived radioisotopes of interest, each target pellet and monitor foil was counted for 200 seconds in the first counting session. The counting sessions following the first were also scheduled according to the half-lives of the radioisotopes (see Table 3.1).

In order to get good counting statistics, high counting rates were preferred. The total system dead time was kept below 10 %. This was accomplished by choosing an appropriate distance between the sample and the detector. A background spectrum was collected before each counting session started. The ORTEC Ge detector was used for the first four counting sessions. The DSG detector was used for counting session 5 when a detector with high resolution was needed to resolve the 514 keV peak of ^{85}Sr and the 511 keV peak.

Table 3.1: Counting sessions for each foil stack

Counting session	Start after EOB	Counting time (seconds)
1	~12 minutes	200
2	2 hours	500
3	24 hours	1200
4	10 days	3600
5	60 days	10800

3.2.4 Data analysis

The average proton energy in each target pellet was calculated using the stopping power formulae of Anderson and Ziegler [And77] presented in Appendix A2. The disintegration data (half lives and branching ratios) of the relevant radioisotopes were obtained from the catalogue of Reus and Westmeier [Reu83].

The peak integration and background subtraction of the relevant γ -ray peaks was achieved by using the peak analysis software EMCAPLUS supplied with the SILENA multi-channel analyzer system. Table 3.2 lists the nuclear reaction products from $^{nat}\text{Rb}+p$ reactions detected in the spectra and for which cross-section data were determined. Strontium-82, however, does not emit γ -rays but it only decays by EC to its daughter ^{82g}Rb ($T_{1/2} = 75$ seconds) which does emit a 776.5 keV γ -ray (absolute abundance = 13.4 %). This γ -ray was used to calculate the ^{82}Sr activity.

Table 3.2: Radioisotopes identified for the $^{nat}\text{Rb}+p$ nuclear reactions and which were measured in this work.

Radioisotopes	Half-life	Energy (keV)	Intensity of major γ -ray (%)
^{77}Br	2.37 days	238.9	23.9
^{80m}Br	4.42 hours	37.1	39
^{79}Kr	35.0 hours	261.3	12.7
^{79}Rb	22.9 min	129.4	10.9
^{81}Rb	4.58 hours	190.2	64.3
^{81m}Rb	30.6 min	86.4	4.72
^{82m}Rb	6.30 hours	554.3	62.5
^{83}Rb	86.2 days	520.4	46
^{84}Rb	32.8 days	881.6	67.9
^{84m}Rb	20.5 min	248.2	63
^{86}Rb	18.7 days	1076.69	8.98
^{80}Sr	1.8 hours	589	39
^{81}Sr	25 min	153.4	35.1
^{82}Sr	25.5 days	776.5	13.4
^{83}Sr	32.2 hours	762.67	30
^{85}Sr	64.7 days	514	99.3
^{85m}Sr	67.7 min	231.78	231.78

As can be seen from the table, this production route produces many by-product radioisotopes. One of these products is the ^{85}Sr radioisotope. The short-lived ^{85m}Sr ($T_{1/2} = 67.7$ minutes) decays by 87 % IT to a longer-lived ^{85}Sr ($T_{1/2} = 64.7$ days) and by 13% EC to stable ^{85}Rb .

The longer-lived ^{85}Sr isotope emits γ -rays with an energy of 514 keV (branching ratio $\varepsilon_{\gamma} = 99.3\%$) which has interference from the positron annihilation peak at 511 keV (see Figure 3.6 (a)). In the figure, it is clear that the FWHM for the 511 keV peak is greater than that of the 514 keV peak (can be explained by Doppler shift). Although a high-resolution detector (DSG-detector) was used, the peaks were still not properly resolved. To accurately determine the areas of these photo-peaks a stripping approach was followed.

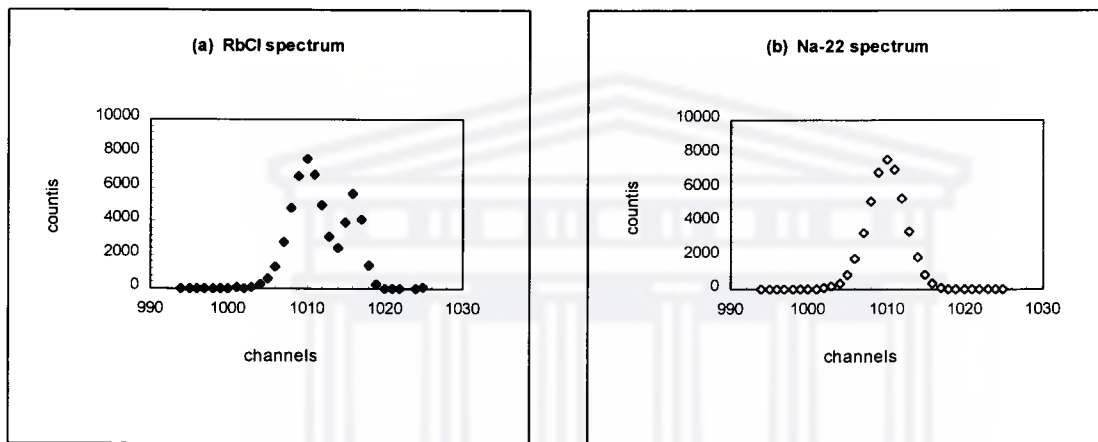


Figure 3.6: Representation of the spectra used in the stripping approach where (a) is the double 511/514 keV peak obtained from RbCl spectrum and (b) is the single 511 keV peak obtained from the ^{22}Na spectrum.

Both the RbCl and the ^{22}Na spectra (Figure 3.6) were recorded under the same detector conditions. After recording the spectra, we checked whether the FWHM of the single 511 keV photo-peak obtained from ^{22}Na was the same as FWHM of the 511 keV photo-peak obtained from RbCl. Regions of interest were marked on the single 511-keV peak obtained from ^{22}Na and on the double 511/514 keV peak obtained from RbCl. Within these regions of interest, the local background subtraction was done. Both the single 511 keV peak (^{22}Na) and the double 511/514 keV peak (RbCl) were normalized and this resulted in the 511 keV of the single-peak (^{22}Na) being exactly the same as the 511 keV of the double 511/514 keV peak (RbCl) (Figure 3.7 (c)). The 511 keV peak was then subtracted from the double (511/514 keV) peak resulting in a single 514 keV peak (Figure 3.7 (d)). The area of the 514 keV peak was then accurately determined.

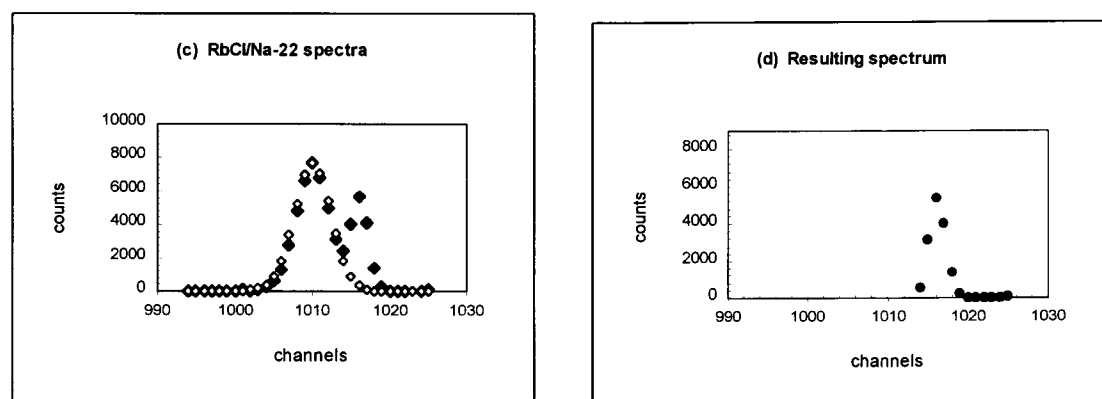


Figure 3.7: Representation of (c) the superimposed RbCl and ^{22}Na spectra (d) the single peak (514 keV) resulting after subtraction of 511 keV peak from the double peak.

3.2.5 Cross-sections and uncertainties

Cross-sections for the production of ^{82}Sr and other by-products in individual pellets were calculated from the measured γ -ray peak areas using the formulae discussed in Appendix A4. The calculated values are listed in Table A6.2. The total uncertainty in each cross-section value was obtained by summing all the contributing uncertainties in quadrature. This total uncertainty consists of a variable component and a constant component.

The variable component comprises the uncertainties in the γ -ray peak areas and in the beam loss compensation. It is necessary to compensate for the fact that some ($< 2\%$) of the incident protons might not reach the last foil of the stack. This is mainly due to nuclear reactions that take place inside the stack, removing protons from the beam and, consequently, causing a beam intensity reduction towards the end of the stack.

The constant part ($\sim 14\%$) includes the uncertainties in the determination of the proton flux (8%), decay correction (1%) and foil thickness (2%). It also includes the uncertainties in the detector efficiency calibration (5%), counting geometry (1%) and photo-peak integration (1%). Additional uncertainties (10%) in the case of ^{85}Sr due to stripping approach were also considered. Uncertainties in the primary proton energy, stopping power and foil thickness

result in an uncertainty in the energy value associated with each data point. All the specified energy values are estimated to be accurate to within 3.0 MeV.

In the spectra there were some spurious photo-peaks, which were not identified due to interference from other γ -rays. For example, a 146.4 keV γ -ray could belong to both ^{77}Kr ($T_{1/2} = 1.24$ hours) and ^{34}Cl ($T_{1/2} = 32$ minutes). Both these γ -rays are emitted with high percentage abundance. In order to be certain to which radioisotope the γ -ray belongs, we have to look at the intensities (branching ratio) of other γ -rays associated with the radioisotopes. In the case of ^{77}Kr , its intense 77 keV and 130 keV lines did not appear in the spectrum at all. On the other hand, the 1176 keV photo-peak for ^{34}Cl did appear but only in the spectra of the first three foils of the 100 MeV stack. Thus, there was no conclusive evidence that the photo-peaks belong to either of those two radioisotopes.

The experimental work discussed in this chapter formed the base of this study. The results and discussions are presented in Chapter 4. They include the excitation function measurement for ^{82}Sr and those of the other radio-contaminants produced.



UNIVERSITY of the
WESTERN CAPE

CHAPTER 4

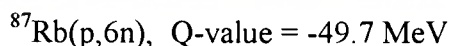
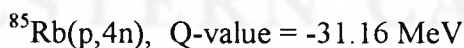
RESULTS AND DISCUSSION

The excitation function measurements for the production of ^{82}Sr and other radio-contaminants in the bombardment of natural rubidium with protons are presented here. These data are compared with previously published data (where applicable) and with the theoretical calculations based on the computer code ALICE-IPPE which is discussed in detail in Appendix A5. The excitation curves presented in the Figures 4.1, 4.4-4.5 show the data obtained in this work, previously published data and ALICE-IPPE calculations. Sections 4.1-4.4 discuss the comparison of the previously published data with those obtained in this work and Section 4.5 discusses the comparison of the ALICE calculations with those obtained in this work. The discussion of the production yields calculated for ^{82}Sr and the production test at high beam currents are presented in Section 4.1.2 and Section 4.1.3.

4.1 Strontium-82

4.1.1 Excitation function

The following reactions contribute to the production of ^{82}Sr via (p,xn) on $^{\text{nat}}\text{Rb}$:



The cross-section values for the production of ^{82}Sr measured in this work are listed in Table A6.2 and the excitation function is shown in Figure 4.1. The data are compared with the published data presented by Deptula *et al.* [Dep90], Horiguchi *et al.* [Hor80] and Lagunas-Solar [Lag93]. The cross-sections presented by Horiguchi *et al.* are for the protons on enriched ^{85}Rb . In order to compare these cross-sections with the data presented in this work they were multiplied by the absolute abundance of ^{85}Rb (72.17%).

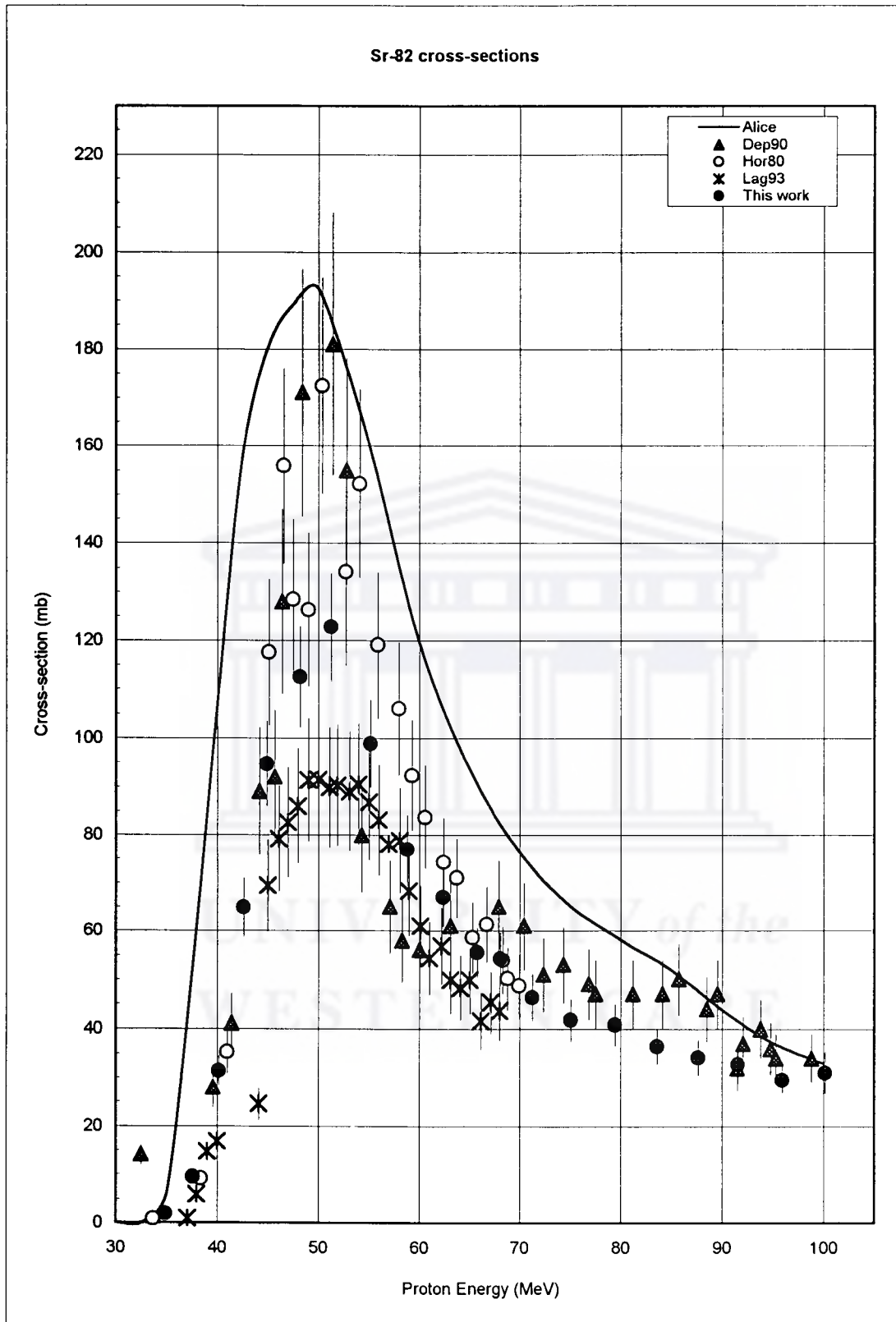


Figure 4.1 : Experimental excitation function for the production of Sr-82 via the (p,xn) reactions on Rb-nat. The data obtained in this work are compared with the theoretical calculations and with those published by Deptula et al. [Dep90], Horiguchi et al. [Hor80] and Lagunas-Solar [Lag93].

In the proton energy region above 60 MeV the agreement is good. In the region around the maximum the cross-sections presented by Deptula *et al.* and Horiguchi *et al.* are higher than the data obtained in this work whereas, the data of Lagunas-Solar are lower than those obtained in this work. The maximum cross-section obtained in this work is 123 mb at $E_p = 50.0$ MeV, 181 mb at $E_p = 51.1$ MeV, 172 mb at $E_p = 50.4$ MeV and 91 mb at $E_p = 51.4$ MeV for Deptula *et al.*, Horiguchi *et al.* and Lagunas-Solar, respectively. The shapes of the peaks of the excitation functions are the same (broad) in the cases of Lagunas-Solar and this work. The peak of the excitation function of the data of Horiguchi *et al.* shows three maximum cross-sections whereas, the peak of Deptula *et al.* is narrow.

4.1.2 Calculated yields based on the excitation function

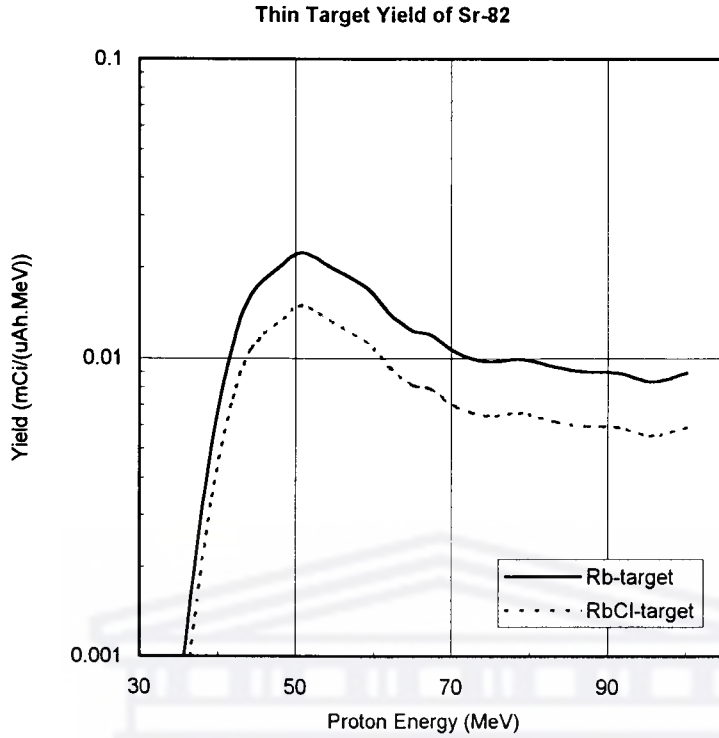
Yields were calculated using the formulae discussed in Appendix A4. The calculated values are listed in Table A6.5 and A6.6. Figure 4.2 shows the ^{82}Sr yields calculated for Rb and RbCl targets. The yield for the RbCl-target was obtained by multiplying the thin target yield for the Rb-target by the ratio of the stopping powers for Rb and RbCl and the ratio of their molecular masses. Table 4.1 shows the calculated yields of both target materials for a specific energy window applicable to the NAC production target holder (see Figure 4.3). It is clear that the yield from a RbCl-target is considerably less (28%) than that calculated for the pure Rb-target. This is mainly due to the fact that the number of rubidium atoms per unit volume in the RbCl-target is 29% less than that in a Rb-target.

Table 4.1 Yield calculated for the production of ^{82}Sr in $^{nat}\text{Rb}+p$.

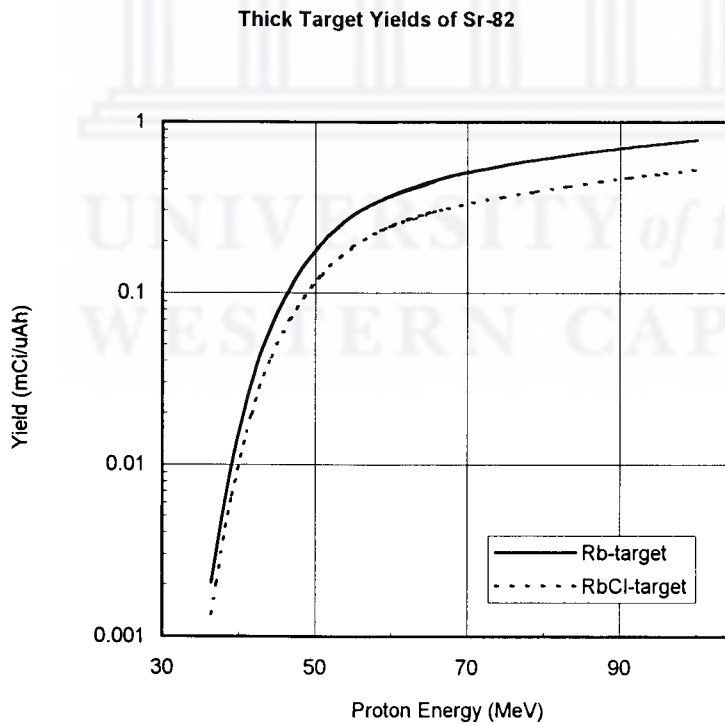
Energy window (MeV)	Target material	Thick-target Yield (mCi/ μAh)
61.5 - 44.0	Rb	0.32
	RbCl	0.23

4.1.3 Production tests at high beam currents

The use of high intensity beams is essential in order to achieve the high production yields required in the production of radioisotopes for use in medicine. In the large-scale production



(a)



(b)

Figure 4.2 : Calculated yields based on the measured excitation functions for the production of Sr-82 by proton bombardment of Rb-nat.

of ^{82}Sr at the NAC cyclotron facility, a thick RbCl target will be bombarded with a 66 MeV proton beam at a nominal intensity of $\sim 100\ \mu\text{A}$. The production team at NAC performed a few production tests that did not form part of this work. Targets were prepared by drying 7g RbCl powder in the oven at $200\ ^\circ\text{C}$ for twenty-four hours. A standard procedure similar to the one in Section 3.2.1 was followed to press thick tablets.

A uni-axial pressure of $5\ \text{tons}/\text{cm}^2$ was applied to the powder for sixty seconds whilst the vacuum pump was still active. The resulting pellet was removed from the system after breaking the vacuum. Each pellet was then heated to $650\ ^\circ\text{C}$ for half an hour after which it was sealed under vacuum in an aluminium capsule (see Figure A1.3) by means of a cold-pressure-welding procedure (see Figure A1.2). The standard aluminium capsule halves were machined from a 6802 grade aluminium alloy and annealed in a laboratory furnace for one hour at $450\ ^\circ\text{C}$. These targets were bombarded with a 66 MeV proton beam and a beam current of up to $90\ \mu\text{A}$ over a period of three to ten hours each. The target arrangement is shown schematically in Figure 4.3.

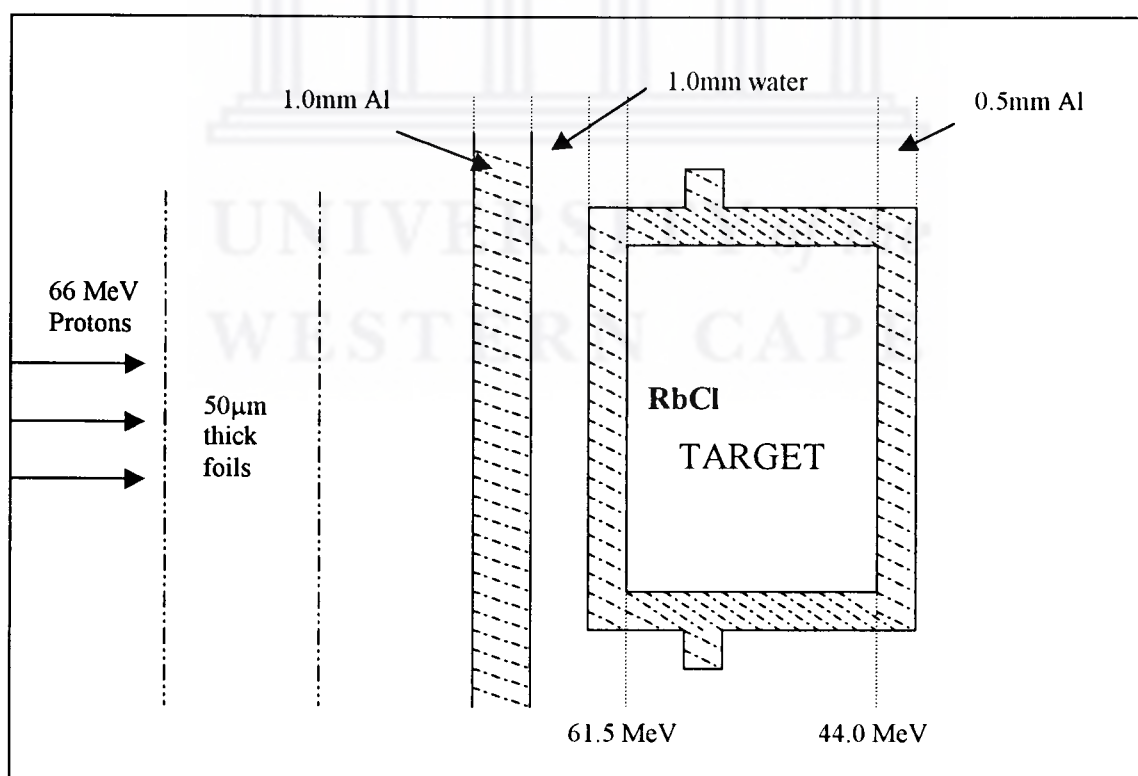


Figure 4.3: Schematic representation of the target arrangement for the production of ^{82}Sr at high currents.

The heat dissipated in the target is of the order of a few kilowatts and it has to be water cooled to prevent thermal failure. After irradiation each target was subjected to a chemical separation procedure. Due to chemical losses the yield in high current production runs is usually lower than the expected value (~ 0.23 mCi/ μ Ah, see Section 4.1.2). This is seen in the cases shown in Table 4.2.

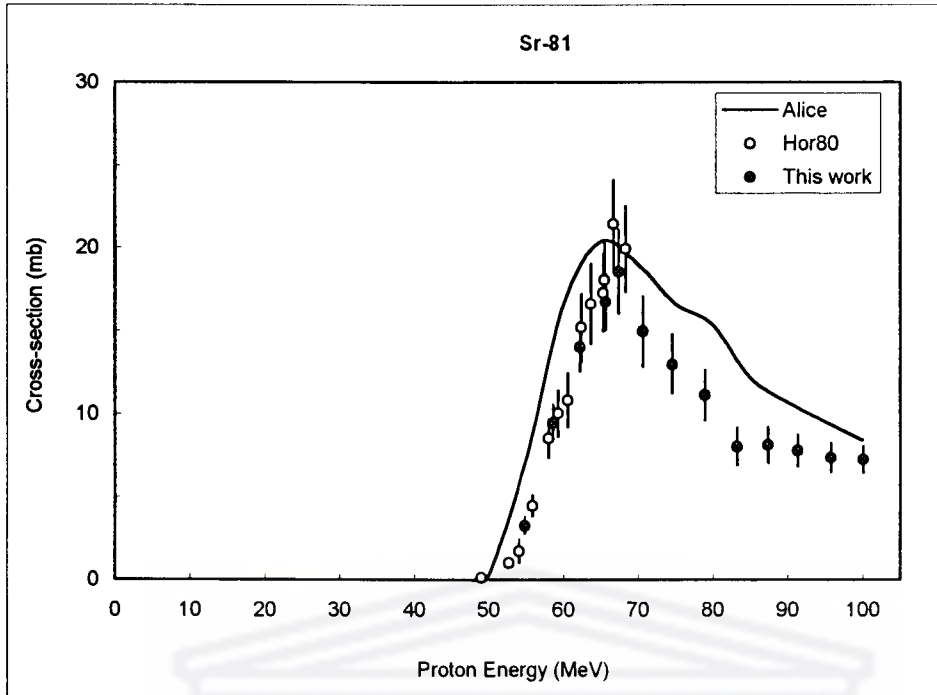
Table 4.2: Production yield of ^{82}Sr measured at end of bombardment (EOB) in production runs at the NAC for the proton-energy window of 44.1-61.5 MeV.

Target No.	Average Current (μA)	Irradiation time (h)	Total Charge (μAh)	Yield at EOB (mCi/ μAh)
2	80	68:52	4997	0.15
6	90	87:54	6785.2	0.15
7	90	69:36	5747	0.13
8	90	50:13	3386	0.13
9	85	77:08	5832	0.12
10	85	126:36	10078	0.15
11	85	136:15	10774	0.16

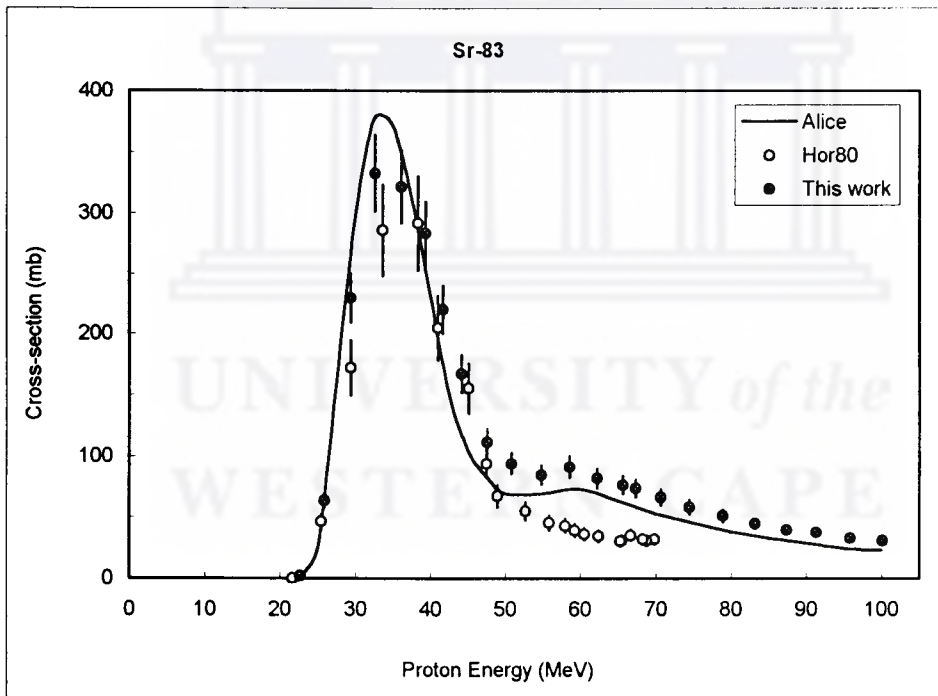
These tests were conducted independently and did not form part of this study. But they confirm that it is possible to get good yields after chemical separation.

4.2 Other strontium radioisotopes

Knowing the excitation functions for the important (p,xn) reactions in $^{nat}\text{Rb}+p$ allows one to accurately determine the amount of each radioisotope impurity expected in the final product of ^{82}Sr . The cross-sections for $^{80,81,83,85}\text{Sr}$ measured in this work are listed in Table A6.2 and the excitation functions are shown in Figures 4.4 and 4.5. The measured cross-sections are for the direct production of the Sr-isotopes via nuclear reactions as presented below:

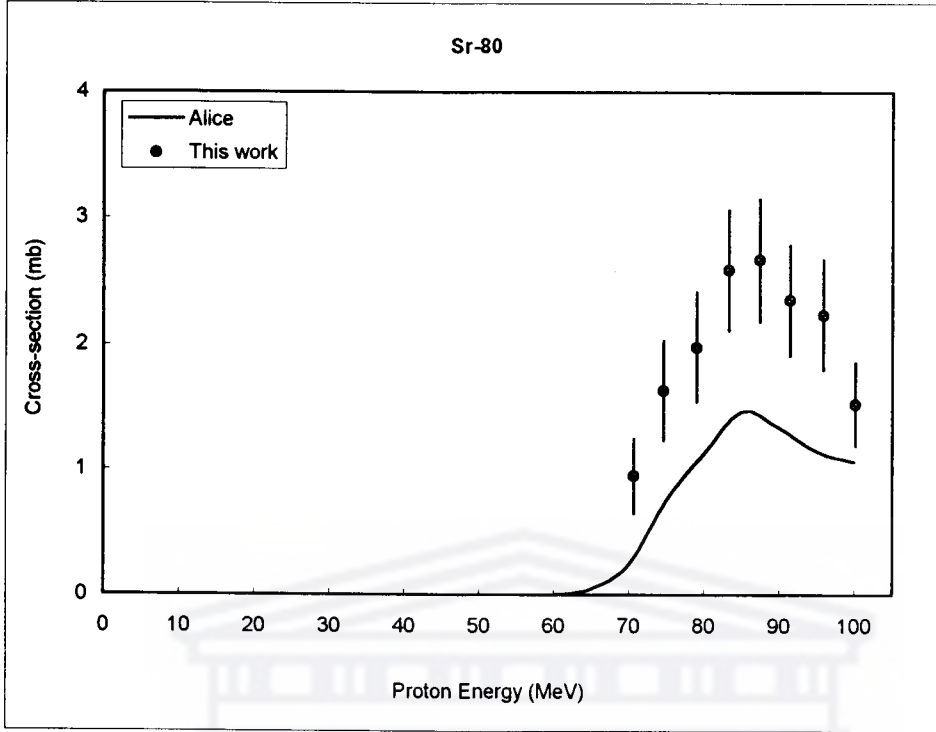


(a)

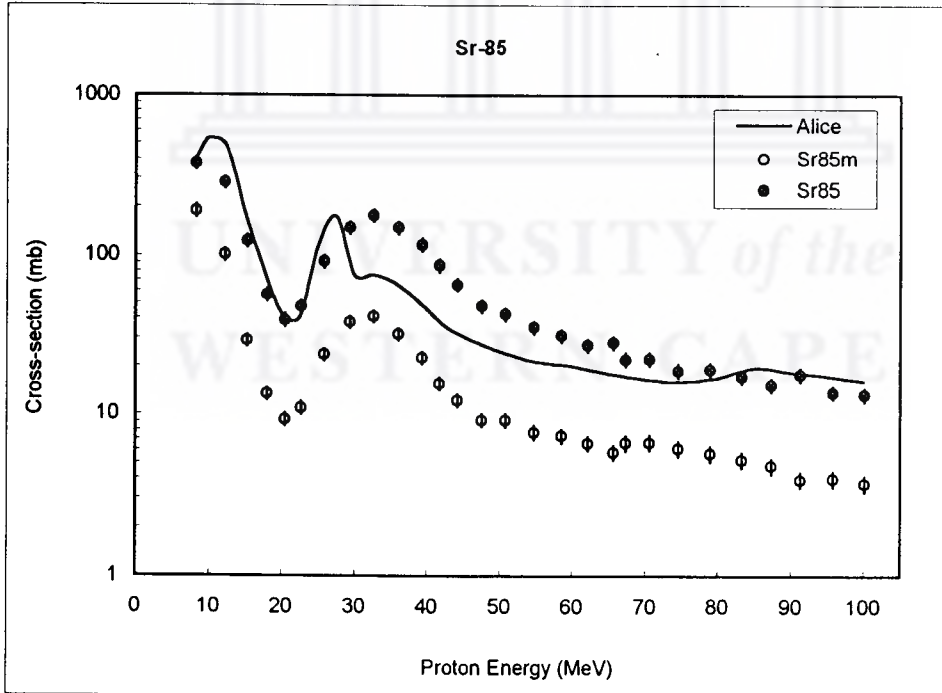


(b)

Figure 4.4: Excitation functions for the production of Sr-81 and Sr-83 via the (p, xn) reactions on Rb-nat. The solid lines represent the theoretical calculations and the points represent the data obtained in this work and the published data of Horiguchi et al. [Hor80].



(a)



(b)

Figure 4.5: Excitation functions for the production of the Sr-80 and Sr-85 via the (p,xn) reactions on Rb-nat. The solid lines represent the theoretical calculations.

^{80}Sr	$^{85}\text{Rb}(p,6n)$	Q-value = -53.0 MeV	^{83}Sr	$^{85}\text{Rb}(p,3n)$	Q-value = -22.3 MeV
	$^{87}\text{Rb}(p,8n)$	-70.7		$^{87}\text{Rb}(p,5n)$	-40.8
^{81}Sr	$^{85}\text{Rb}(p,5n)$	-43.7	^{85}Sr	$^{85}\text{Rb}(p,n)$	-1.84
	$^{87}\text{Rb}(p,7n)$	-64.0		$^{87}\text{Rb}(p,3n)$	-20.4

In the case of $^{81,83}\text{Sr}$, the present measurements are also compared with those for protons on enriched ^{85}Rb published by Horiguchi *et al.* [Hor80]. The data of Horiguchi are multiplied by the absolute natural abundance of ^{85}Rb (72.17%) so that they could be compared with the data obtained in this work in the applicable energy region.

In the case of $^{81,83}\text{Sr}$, the agreement between the data obtained in this work and the data of Horiguchi *et al.* is very good except for the case of ^{83}Sr , where in the proton energy above 50 MeV there is a discrepancy between the data. In this region the data of Horiguchi *et al.* are lower than the data obtained in this work. This is explained by the contribution of the $^{87}\text{Rb}(p,5n)$ reaction (Q-value = -41 MeV) in the natural target. Also, in the excitation function for ^{85}Sr the contribution by both the $^{85,87}\text{Rb}$ targets is evidenced by the two maxima, where the first one is due to the $^{85}\text{Rb}(p,n)$ reaction and the second maximum is due to the (p,3n) reaction on ^{87}Rb . Both $^{80,81}\text{Sr}$ reach their maxima at higher energies due to their higher reaction Q-values. The contribution by the ^{87}Rb in the natural target is seen in the excitation functions of $^{83,85}\text{Sr}$. In each case a second peak is visible at higher proton energies.

4.3 Rubidium radioisotopes

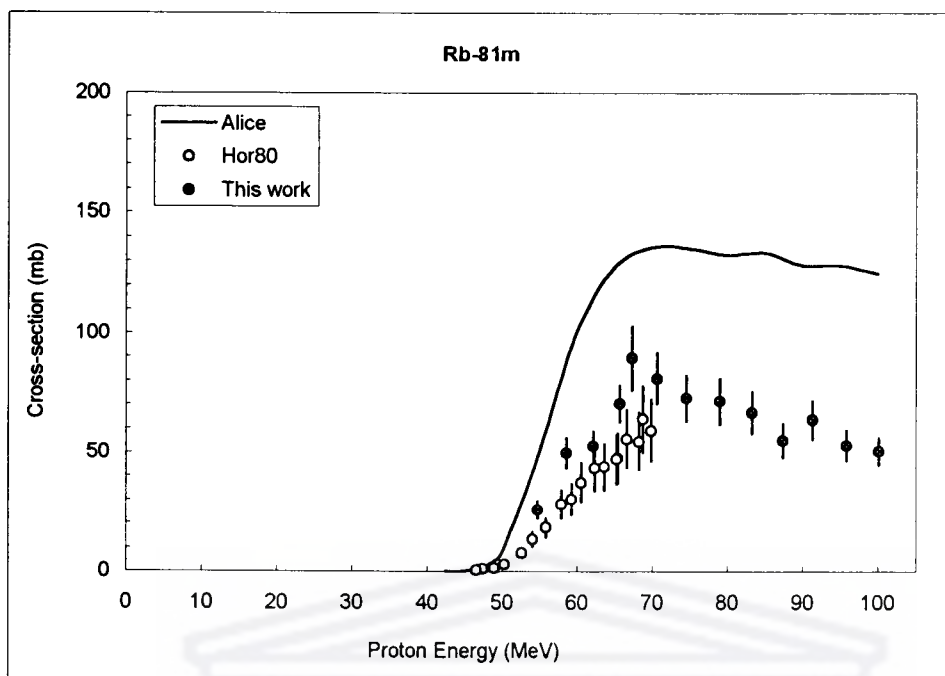
Rubidium isotopes can be produced either by the direct formation via nuclear reactions or via the decay of their precursors. The cross-sections measured in this work and the excitation functions presented are for the following possible reactions:

^{79}Rb	$^{85}\text{Rb}(p,p6n)$	Q-value = -48.4 MeV
	$^{85}\text{Rb}(p,7n)^{79}\text{Sr}$	-49.2
	$^{87}\text{Rb}(p,p8n)$	-64.5
	$^{87}\text{Rb}(p,9n)^{79}\text{Sr}$	-65.4
^{81}Rb	$^{85}\text{Rb}(p,p4n)$	-38.9
	$^{85}\text{Rb}(p,5n)^{81}\text{Sr}$	-41.9

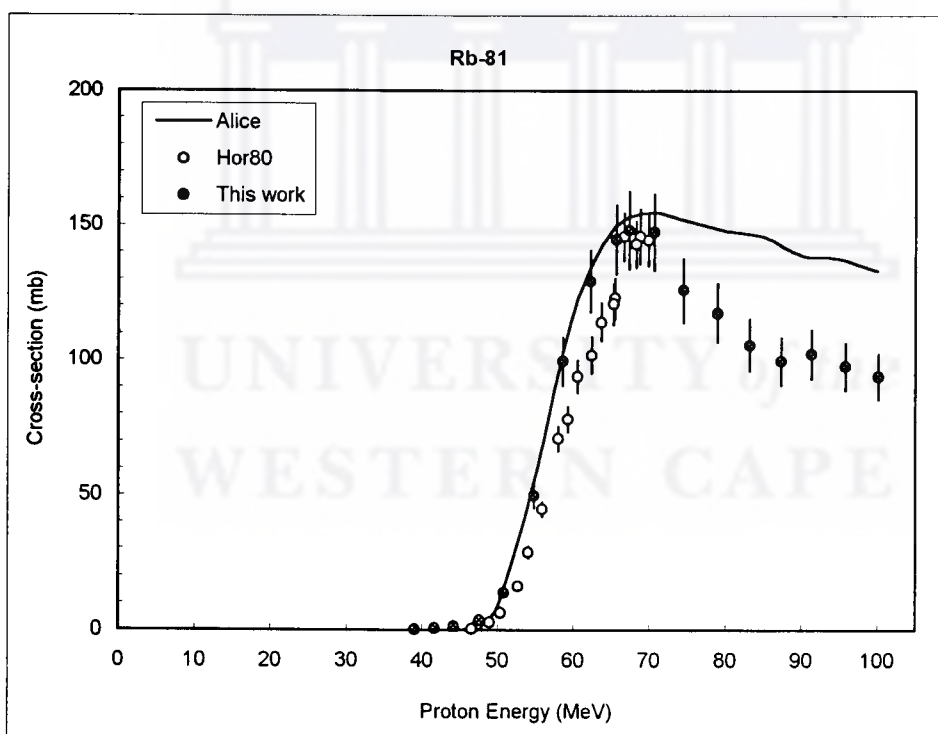
^{81}Rb	$^{87}\text{Rb}(p,p6n)$	Q-value = -58.4 MeV
	$^{87}\text{Rb}(p,7n)^{81}\text{Sr}$	-49.3
^{82m}Rb	$^{85}\text{Rb}(p,p3n)$	-30.2
	$^{87}\text{Rb}(p,p5n)$	-48.7
^{83}Rb	$^{85}\text{Rb}(p,p2n)$	-19.2
	$^{85}\text{Rb}(p,3n)^{83}\text{Sr}$	-22.3
^{83}Rb	$^{87}\text{Rb}(p,p4n)$	-37.8
	$^{87}\text{Rb}(p,5n)^{83}\text{Sr}$	-40.8
^{84}Rb	$^{85}\text{Rb}(p,pn)$	-10.5
	$^{87}\text{Rb}(p,p3n)$	-29.1
^{86}Rb	$^{87}\text{Rb}(p,pn)$	-9.9

The cross-section values are listed in Table A6.3 and the excitation functions are shown in Figures 4.6 to 4.9. In Figures 4.6 to 4.8 the data obtained in this work are also compared with those for protons on enriched ^{85}Rb published by Horiguchi *et al* [Hor80]. The data of Horiguchi *et al.* are multiplied by the absolute natural abundance of ^{85}Rb in order to compare them with the data obtained in this work at the applicable proton energies. Also in the cases of $^{83,84}\text{Rb}$ the results presented by Horiguchi did not include the contribution by the decay of ^{83}Sr and ^{84m}Rb . Hence, in order to compare with our results we had to add those contributions.

In the cases of $^{81,81m,82m,83}\text{Rb}$ the comparison between the data obtained in this work and the data of Horiguchi *et al.* is reasonably good except for the apparent energy shift in the case of ^{83}Rb . Indications of the slight energy shift are also visible in the case of ^{81}Rb . In the excitation functions of ^{84}Rb and ^{84m}Rb , around the peak regions (20-50 MeV) the data of Horiguchi *et al.* are significantly higher than the data obtained in this work but above 50 MeV the agreement is good in the case of ^{84m}Rb and excellent in the case of ^{84}Rb . The reason for the discrepancy at energies below 50 MeV is that perhaps Horiguchi *et al.* had other contaminants. The contribution by the ^{87}Rb in the natural target is seen in the excitation functions of $^{82m,83,84}\text{Rb}$. In each case a second peak is visible at higher proton energies. This is also noticeable in the excitation function of ^{86}Rb . Obviously these second peaks are not visible in the data of Horiguchi *et al.*

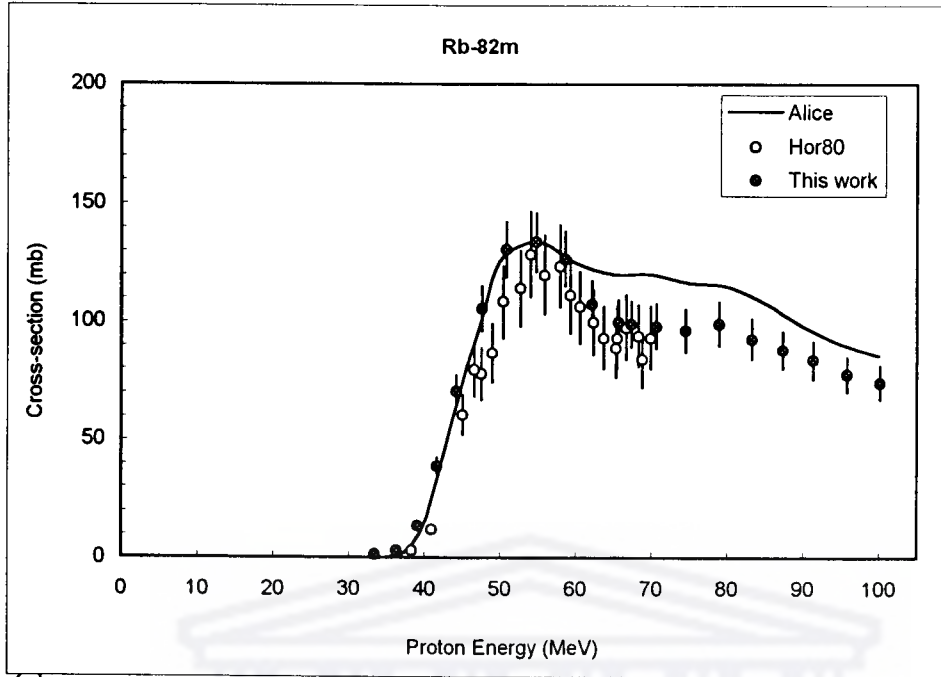


(a)

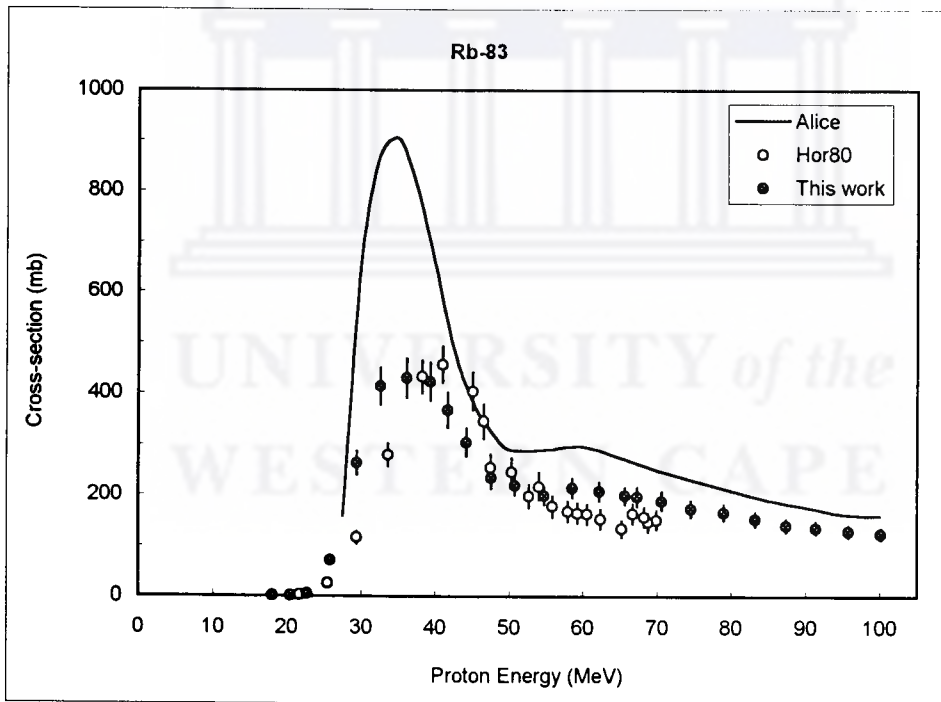


(b)

Figure 4.6: Excitation functions for the production of Rb-81 in the proton bombardment of Rb-nat. The solid lines represent the theoretical calculations and the points represent the data obtained in this work and the published data of Horiguchi et al. [Hor80].

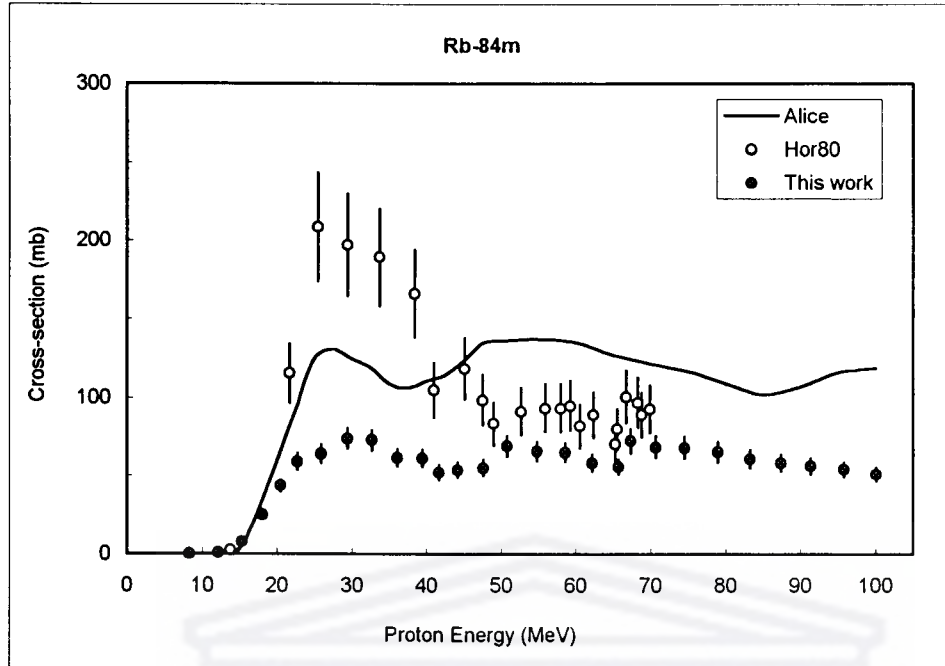


(a)

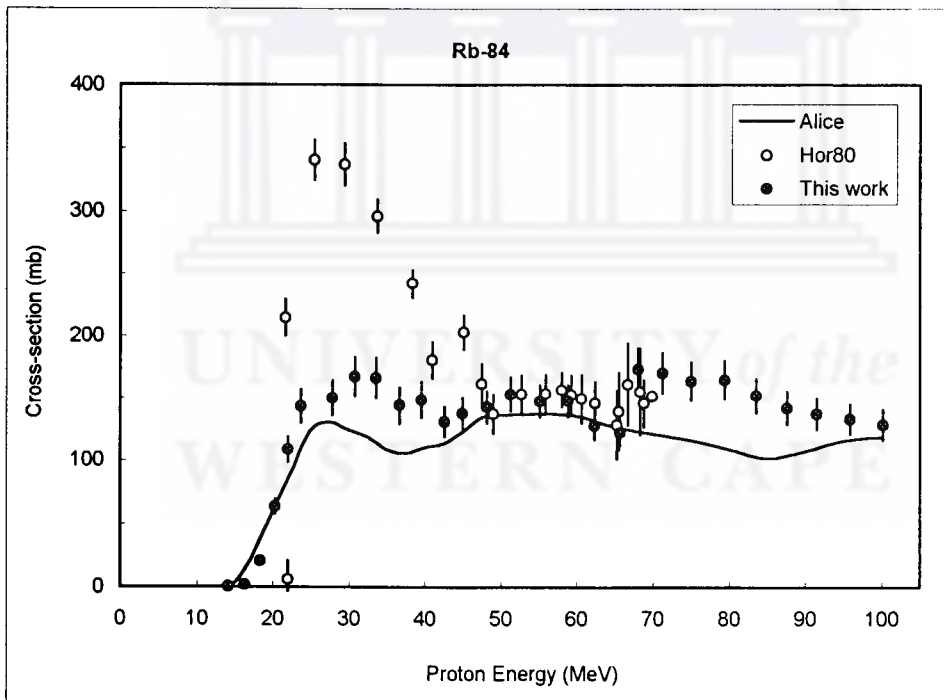


(b)

Figure 4.7: Excitation functions for the production of Rb-82 and Rb-83 in the proton bombardment of Rb-nat. The solid lines represent the theoretical calculations and the points represent the data obtained in this work and the published data of Horiguchi et al. [Hor80].

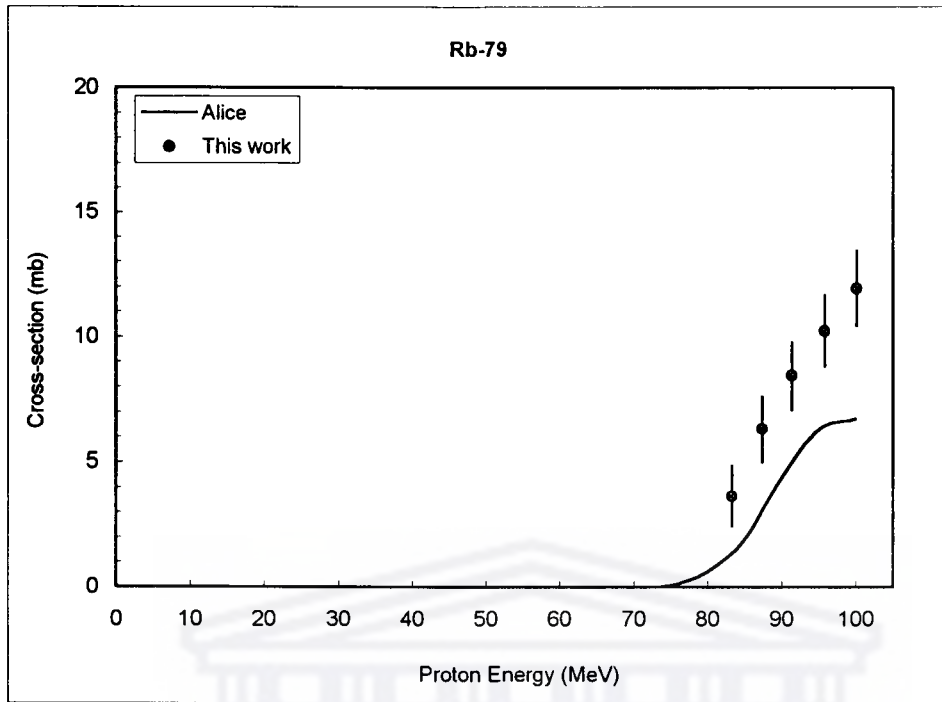


(a)

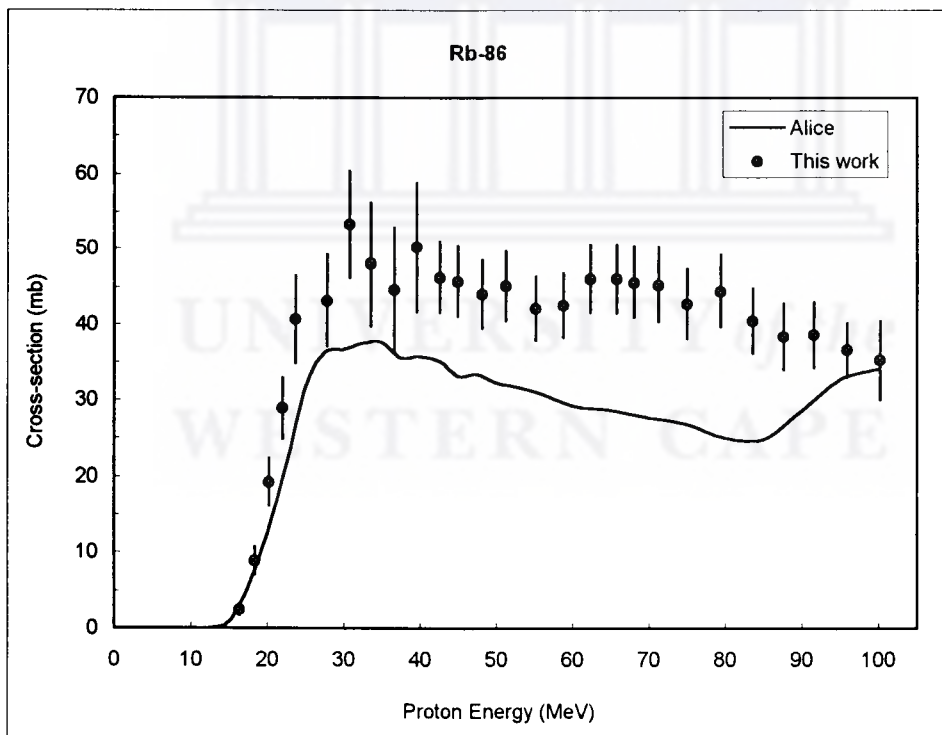


(b)

Figure 4.8: Excitation functions for the production of Rb-84 in the proton bombardment of Rb-nat. The solid lines represent the theoretical calculations and the points represent the data obtained in this work and the published data of Horiguchi et al. [Hor80].



(a)



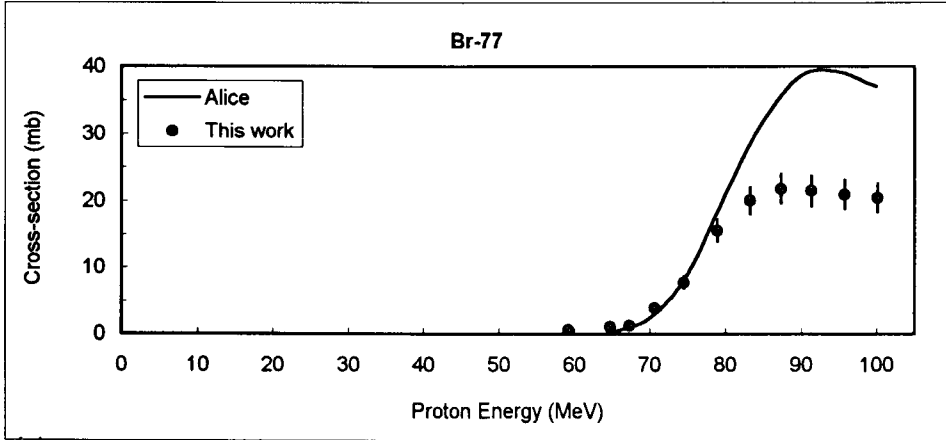
(b)

Figure 4.9: Excitation functions for the production of Rb-79 and Rb-86 in the proton bombardment of Rb-nat. The solid lines represent the theoretical calculations.

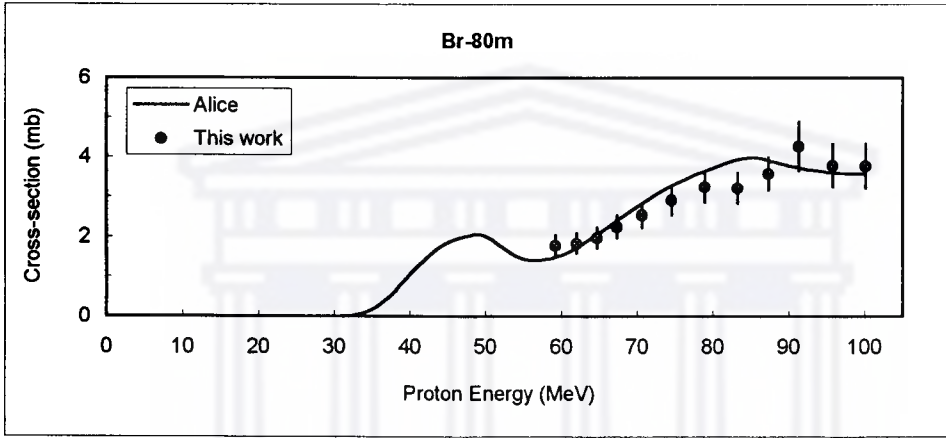
4.4 Bromine and krypton radioisotopes

The cross-section measurements for Br and Kr radioisotopes are listed in Table A6.4 and the excitation functions are shown in Figure 4.10. Some of these radioisotopes are produced either directly or via the decay of their precursors. The cross-sections measured in this work include all the reactions listed below:

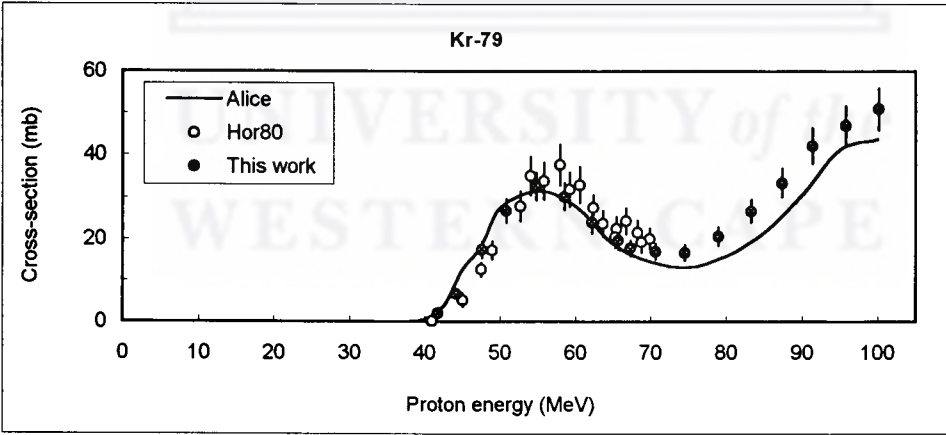
^{77}Br	$^{85}\text{Rb}(p,3p6n)$	Q-value = -62.9 MeV
	$^{85}\text{Rb}(p,\alpha p4n)$	-43.6
	$^{85}\text{Rb}(p,2p7n)^{77}\text{Kr}$	-63.8
	$^{85}\text{Rb}(p,\alpha 5n)^{77}\text{Kr}$	-47.5
	$^{85}\text{Rb}(p,9n)^{77}\text{Sr}$	-63.3
	$^{85}\text{Rb}(p,p8n)^{77}\text{Rb}$	-64.5
	$^{87}\text{Rb}(p,3p8n)$	-83.8
	$^{87}\text{Rb}(p,\alpha p6n)$	-65.4
	$^{87}\text{Rb}(p,2p9n)^{77}\text{Kr}$	-82.0
	$^{87}\text{Rb}(p,\alpha 7n)^{77}\text{Kr}$	-66.5
	$^{87}\text{Rb}(p,11n)^{77}\text{Sr}$	-77.4
	$^{87}\text{Rb}(p,p10n)^{77}\text{Rb}$	-80.6
$^{80\text{m}}\text{Br}$	$^{85}\text{Rb}(p,3p3n)$	-45.1
	$^{85}\text{Rb}(p,\alpha pn)$	-16.8
	$^{87}\text{Rb}(p,3p5n)$	-75.1
	$^{87}\text{Rb}(p,\alpha p3n)$	-50.4
^{79}Kr	$^{85}\text{Rb}(p,2p5n)$	-45.5
	$^{85}\text{Rb}(p,\alpha 3n)$	-27.1
	$^{85}\text{Rb}(p,7n)^{79}\text{Sr}$	-49.2
	$^{85}\text{Rb}(p,p6n)^{79}\text{Rb}$	-48.4
	$^{87}\text{Rb}(p,2p7n)$	-63.7
	$^{87}\text{Rb}(p,\alpha 5n)$	-45.6
	$^{87}\text{Rb}(p,9n)^{79}\text{Sr}$	-65.4
	$^{87}\text{Rb}(p,p8n)^{79}\text{Rb}$	-64.5



(a)



(b)



(c)

Figure 4.10: Excitation functions for the production of Br-77, Br-80m and Kr-79 on the proton bombardment of Rb-nat. The solid lines represent the theoretical calculations and the points represent the data obtained in this work and the published data of Horiguchi et al. [Hor80].

There was no available previously published data to compare the excitation function of $^{77,80\text{m}}\text{Br}$ with. These excitation functions show the high-energy cross-section maxima. In the case of ^{79}Kr , the excitation function is compared with the previously published data of Horiguchi *et al.* [Hor80]. The data of Horiguchi *et al.* was multiplied by the absolute natural abundance of ^{85}Rb for this purpose. The comparison is excellent especially since no precautions were taken in order to avoid the gaseous krypton from escaping.

4.5 Comparison with theoretical calculations by means of ALICE-IPPE

The ALICE-IPPE, [Bla89], calculations are compared with the data obtained in this work. These calculations include both metastable states and ground states. The agreement between the ALICE-IPPE values and the data obtained in this work is excellent in the cases of $^{81,83}\text{Sr}$, $^{81,82\text{m},84,86}\text{Rb}$, $^{80\text{m}}\text{Br}$ and ^{79}Kr . But there is a noticeable slight energy shift in the excitation function of ^{85}Sr and the agreement is worst. Also, in the excitation functions of ^{81}Rb at proton energies above the maximum cross-section the ALICE-IPPE values are slight higher but below a factor of 2. The shape of the excitation functions of $^{80,82}\text{Sr}$ and $^{79,83}\text{Rb}$ obtained in this work is the same as that of the ALICE-IPPE data but the calculated values are higher by a factor $1.5 < f < 2$. The reasons are unclear. In the case of the excitation function of ^{84}Rb the agreement is good at proton energies around 42-70 MeV and below 21 MeV. In the regions between 21-42 MeV and above 70 MeV there ALICE-IPPE values are lower by a factor of 1.5. This is also noticeable in the excitation function of ^{86}Rb where the agreement is reasonable below 40 MeV and then there is a considerable drop in the ALICE-IPPE calculated values. The drop in the cross-section of the ALICE-IPPE values changes the shape of the excitation function. The reason(s) for the discrepancy in the excitation function of ^{83}Rb are unclear. In this case the ALICE-IPPE values are higher by a factor of 2.2. In summary, ALICE-IPPE calculated values compare well with the data obtained in this work with just a few exceptions.

The total number of excitation functions measured in this work is fourteen, where five of those are for strontium radioisotopes, including ^{82}Sr . Six excitation functions for the production of rubidium isotopes, three of the bromine isotopes and one for a krypton isotope are also included. Some general conclusions and a few suggestions are presented in the following chapter.

CHAPTER 5

CONCLUSION

The main aim of this study was the determination of excitation functions for $^{nat}\text{Rb}+p$ with an emphasis on the production of ^{82}Sr and other radio-strontiums. This was done by measuring the production cross-sections for proton energies up to 100 MeV. The purpose was to study the problems that are posed by other radio-strontiums in the final ^{82}Sr product. The relevant excitation functions were used to maximize its production yield given constraints on energy range, target thickness and the impurity levels. The excitation functions were measured by means of the stacked-foil technique. Three stacks with incident proton energies of 100.1, 66.8 and 40.4 MeV were used in order to minimize energy spread in the low-energy region. The production yields of ^{82}Sr were calculated from the excitation function.

In the case of ^{82}Sr experimental data published previously by Deptula *et al.*, Lagunas-Solar and Horiguchi *et al.* were used for comparison purposes. Theoretical calculations using the code ALICE-IPPE were also compared with the data obtained in this study. Of the three published data sets found, two sets focus on the production of ^{82}Sr via the $^{nat}\text{Rb}(p,xn)$ nuclear reactions and were published by Deptula *et al.* and Lagunas-Solar. The third data set in the literature presented by Horiguchi *et al.* derived the ^{82}Sr cross-sections from the $^{85}\text{Rb}(p,4n)$ nuclear reaction. There are significant discrepancies between these published data sets especially at the peak. The data published by Deptula *et al.* are higher than the data presented by Lagunas-Solar by almost a factor of 2. The present data lie between the extremes of the published data. The maximum cross-sections of Deptula *et al.*, Horiguchi *et al.* and Lagunas-Solar are: 1.5, 1.2 and 0.74 times the maximum cross-section of the present data. All data sets have similar uncertainties: Deptula's are 15%, Horiguchi's are 15-16% and Lagunas-Solar are 14%. A final feature worth commenting on is the width of the peak. The peak of the excitation function of the data published by Deptula *et al.* is narrow (~ 8 MeV) whereas, the peak of the excitation function of the data sets published by Lagunas-Solar, Horiguchi and the present work is broad (~ 15 MeV).

In comparing published excitation functions with the data obtained in this work the agreement is good at proton energies above 60 MeV. The shape of the peak of the excitation

function obtained in this work seems to support the data presented by Lagunas-Solar with its broader peak. The broadness of the peak is also supported by the ALICE-IPPE calculated values. The cross-sections calculated from ALICE-IPPE are even larger than the highest reported experimental values. At the peak ALICE-IPPE calculated values are higher than the values obtained in this present study by a factor of 1.6.

The agreement between the experimental and theoretical values for the maximum cross-section is poor. This conclusion is based on the discrepancies found on the data. The lack of previously published data does not help. The confirmation of the shape of the peak of the excitation function is the only positive result drawn from the comparisons.

Figure 5.1 shows the excitation functions obtained in the present study for the strontium radioisotopes up to 100 MeV. The figure clearly shows that the short-lived isotopes $^{80,81}\text{Sr}$ only occur in the high-energy region (over 55 MeV). The excitation functions for ^{83}Sr covers the region from 20-100 MeV while that of ^{85}Sr covers the region from 5-100 MeV. The excitation function for ^{82}Sr has a maximum around 40-60 MeV. It is impossible to select an energy window in which the ^{82}Sr cross-section is much greater than those of $^{83,85}\text{Sr}$. From the figure it is clear that a good choice is around 40 to 60 MeV where the ^{82}Sr cross-section is maximum and the cross-sections for the longer lived strontium contaminants ($^{83,85}\text{Sr}$) have decreased from their maximum.

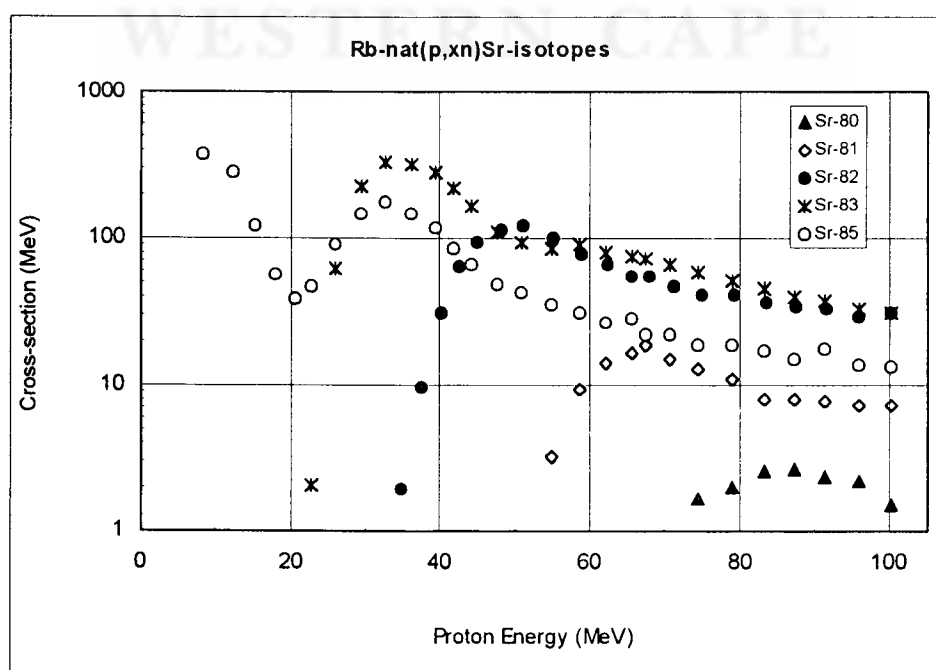


Figure 5.1: Excitation functions for the strontium isotopes

In this study the activity of $^{82,83,85}\text{Sr}$ was calculated for the energy window 44.1-61.5 MeV with a charge of 1 μAh . This window was chosen because it is commonly used at the NAC. At EOB (end of bombardment) the activity of the $^{82,83,85}\text{Sr}$ are given in Table 5.1 below.

Table 5.1: Activities of radioisotopes at different times after EOB as observed in the irradiation of ^{nat}Rb with protons in the production energy window 44.1-61.5 MeV for 1 μAh .

Isotope	Half-life (days)	Activity (mCi)					
		EOB	5 days	10 days	15 days	20 days	25 days
^{82}Sr	25.6	0.233	0.203	0.177	0.155	0.135	0.118
^{83}Sr	1.35	4.11	0.311	0.0242	0.00186	0.000143	1.097×10^{-5}
^{85}Sr	64.8	0.0142	0.0135	0.0128	0.0121	0.0115	0.0109

From the table it is clear that ^{83}Sr does not pose a major problem after 15 days of decay. At EOB the ratio of ^{85}Sr to ^{82}Sr is ~ 0.061 . At 5 days after EOB this ratio would have increased to ~ 0.066 . The ratio would continually increase until say 25 days after EOB it is ~ 0.0922 . By carefully choosing the exit energy one can minimise the amount of ^{85}Sr in the product.

In the bombardment of ^{nat}Rb with protons, the final ^{82}Sr product at 15 days after EOB contains about 7.8 % ^{85}Sr . This is not the case for the production of ^{82}Sr via the $^{nat}\text{Mo}(p,\text{spall})$ nuclear reactions. In the spallation of ^{nat}Mo targets there are two additional long-lived radiostrontiums present in the final product namely, ^{89}Sr ($T_{1/2} = 50.5$ days) and ^{90}Sr ($T_{1/2} = 28.5$ years), making the bombardment of ^{nat}Rb with protons a better production method.

In the cases of all radio-contaminants, the published data of Horiguchi *et al.* was compared with the data obtained in the present study. The data presented by Horiguchi *et al.* was for protons on enriched ^{85}Rb and therefore, it was multiplied by the natural abundance of ^{85}Rb (72.17%). The one disadvantage of using enriched materials is that the contribution of other reactions is not studied. There is excellent agreement between the published data and the data

obtained in this work in cases of ^{81}Sr , ^{82}Rb , and ^{79}Kr . In the case of ^{79}Kr , no precautions were taken (in this work) to avoid the escape of gaseous krypton. Even so, the published data agrees well with our data. In the cases of ^{83}Sr the agreement is good at proton energies below 50 MeV. Above that energy region there are discrepancies caused by differences in target material used. The data of Horiguchi *et al.* do not show the second peak which is due to the contributions of ^{87}Rb in the natural target. In the cases of $^{81\text{m},81}\text{Rb}$ there is a noticeable energy shift. The agreement is still good. There is a prominent energy shift in the case of ^{83}Rb and the reasons are unclear. The agreement in the case of $^{84\text{m},84}\text{Rb}$ is poor. The shapes of the excitation functions are not the same. The cross-sections presented by Horiguchi *et al.* show noticeable irregularities.

The agreement between the calculated ALICE-IPPE values and the data obtained in this work is good in the cases of $^{81,83}\text{Sr}$, $^{82,84}\text{Rb}$, $^{80\text{m}}\text{Br}$ and ^{79}Kr . In other cases such as $^{80,85}\text{Sr}$, $^{79,81,86}\text{Rb}$ and ^{77}Br the agreement is not as good but is within a factor of 2. In ^{83}Rb the agreement is slightly worse with ratios of up to 2.2 between the data sets.

In summary, all the non-isotopic radio-contaminants ($^{79,81\text{m},82,83,84\text{m},84}\text{Rb}$, $^{77,80\text{m}}\text{Br}$ and ^{79}Kr) do not pose a problem in the ^{82}Sr final product since all can be chemically separated from ^{82}Sr . In addition most are short-lived isotopes.

In the case of the thick target tests conducted at the NAC it was found that good yields were achieved by bombarding a thick RbCl-target (7 g) with a proton beam of 66 MeV at $\sim 100 \mu\text{A}$ intensity. Thick target yields of 0.12 - 0.16 mCi/ μAh for the production energy window of 44.1 - 61.5 MeV were obtained. This supports the yield of 0.23 mCi/ μAh calculated from the measured excitation function especially if one takes into account the losses due to chemical separation. This exercise confirmed that this energy range is suitable for the production of ^{82}Sr . The 66 MeV routine production proton beam available at the NAC can therefore be used for the production of ^{82}Sr via the $^{\text{nat}}\text{Rb}(p,xn)$ nuclear reactions.

For future work, it is recommended that one should use a thick target (7g) as used in production runs but at low current intensities of 0.1 μA and at different exit energies. The results should be compared with those data obtained in production runs. Also, the use of enriched ^{85}Rb targets with the thickness of 200 mg/cm^2 used at 0.1 μA currents would be good for comparing with the present data set.



APPENDIX A1

SCHEMATIC ILLUSTRATIONS OF THE TOOLS FOR THE PRESSING AND SEALING OF TABLETS

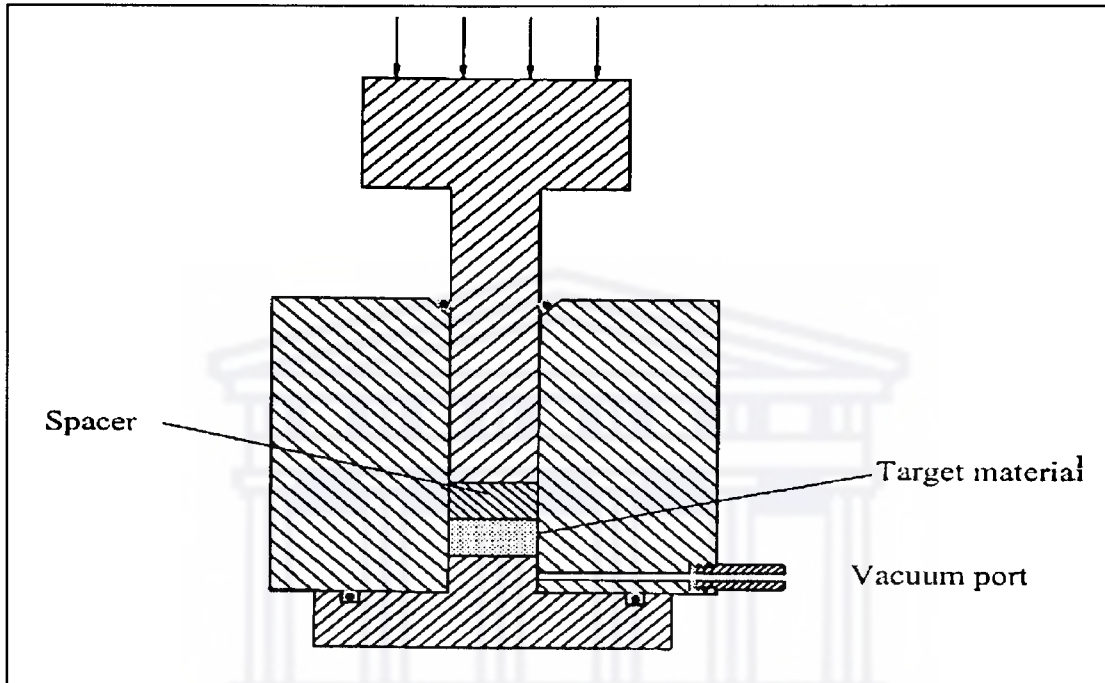


Figure A1.1: Schematic diagram of the punch-and-die set used for pressing tablets at the NAC cyclotron facility.

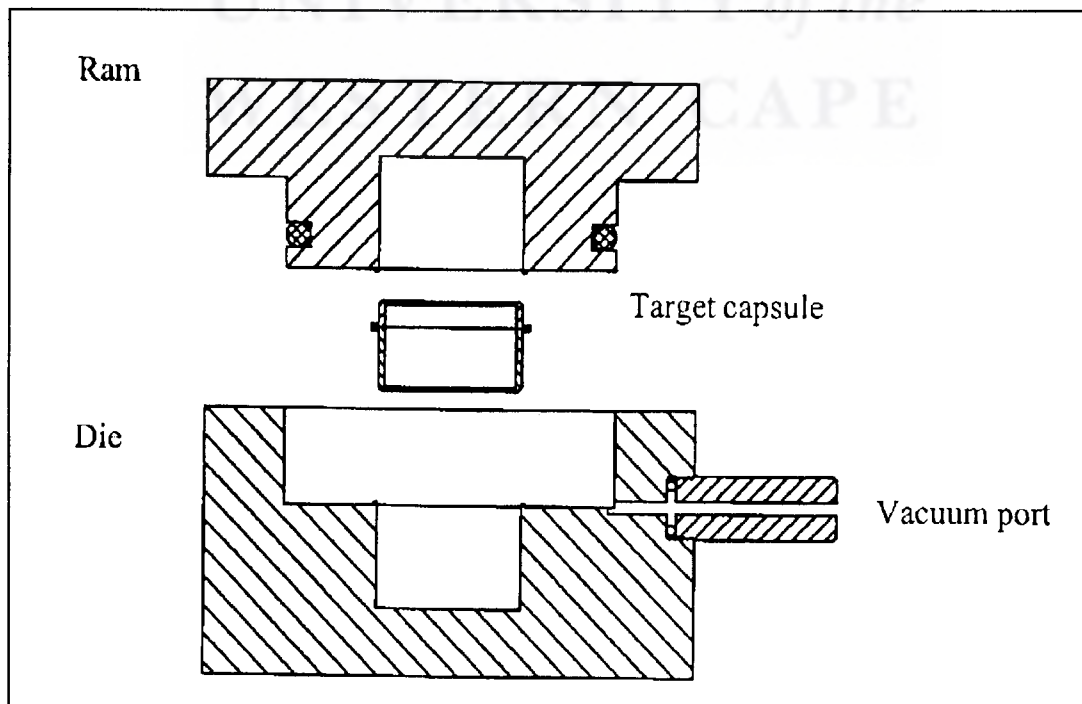


Figure A1.2: Schematic representation of the cold-pressure-welding tool.



Figure A1.3 A thick target pellet of 7 g in mass and 20 mm in diameter prepared at the NAC for the production of ^{82}Sr . The target is sealed in an aluminium capsule.

APPENDIX A2

CALCULATION OF STOPPING POWER

The stopping power calculations for elements were based on the expressions presented by Anderson and Ziegler [And77] for hydrogen (protons, deuterons and tritons) in elements. It concerns a semi-empirical parameter fits for elements from the Bethe-formula. The expression treats three energy regions separately. These regions are, (a) the high-energy region (particle energy above 1 MeV/nucleon), (b) the low-energy region (particle energy 1-10 keV/nucleon) and (c) the intermediate region (particle energy between 10-1000 keV/nucleon).

At medium and high-energy range the Bethe equation is given by:

$$S(E) = \frac{4\pi e^4 Z_1^2 Z_2^2}{mv^2} L(v, Z_2) \quad (\text{A2.1})$$

Where $L = (v, Z_2) = L_0$

$$= \ln\left(\frac{2mv^2}{I}\right) - \ln(1 - \beta^2) - \beta^2 - \frac{C}{Z_2}$$

Whereby $\beta = v/c$ with v and c the particle velocity and the velocity of light; m and e are the electron mass and charge respectively, Z_1 is the atomic number of the projectile; Z_2 is the atomic number of the target element. The main parameters of the Bethe-formula are the mean ionization I , which characterizes the target, and the shell correction term C/Z_2 for low energy correction. The parameter β is related to the kinetic energy E of the projectile by:

$$\beta^2 = 1 - \left[1 + \frac{E}{931100}\right]^{-2} \quad (\text{A2.2})$$

This expression was used as a model for fitting the experimental stopping power for protons in elements for energies >1 MeV/nucleon so that it can be written as:

$$S(E) = \left(\frac{A_6}{\beta^2} \right) \left[\ln \left[\frac{A_7 \beta^2}{1 - \beta^2} \right] - \beta^2 - \sum_{i=0}^4 A_{i+8} (\ln E)^i \right] \quad (\text{A2.3})$$

This formula in addition to the stopping power for intermediate and low-energy ranges given by

$$S = A_1 E^{0.5}, (1-10\text{keV}) \quad (\text{A2.4})$$

$$S^{-1} = \frac{1}{S_{\text{low}}} + \frac{1}{S_{\text{high}}}, (10-100\text{keV}) \quad (\text{A2.5})$$

Where $S_{\text{low}} = A_2 E^{0.45}$ and $S_{\text{high}} = \frac{A_3}{E} \ln \left(1 + \frac{A_4}{E} + A_5 E \right)$, respectively.

The proton energy E is given in eV and the A_j 's are fitting parameters of which their values were taken from the tables of [And77]. The stopping power S is given in eV/(10^{15} atoms/cm²).

For compounds, the stopping power is given by the "additivity rule" of Bragg-Kleeman as referred to [Hel83]. If one considers a target composed of components A and B, then the stopping power is given by the summation of the independent stopping powers of the two components as:

$$S(A_n, B_m) = nS(A) + mS(B) \quad (\text{A2.6})$$

Where n and m are the relative mass, concentration of each component where $n+m=1$.

All the stopping power and energy calculations were carried out with the computer by the programs STOPPING and STACK which incorporated the above-mentioned formulae.

APPENDIX A3

CALCULATION OF REACTION Q-VALUES

The minimum energy require for a reaction to start is known as the “Q-value” of the reaction. As mentioned in Section 2.2.2, this quantity balances the masses before and after the reaction.

It is expresses as

$$Q = (m_{\text{initial}} - m_{\text{final}}) c^2 \quad (\text{A3.1})$$

where the initial masses are given by

$$m_{\text{initial}} = m_{\text{projectile}} + m_{\text{target}} \quad (\text{A3.2})$$

and the final masses are given by

$$m_{\text{final}} = m_{\text{ejectile}} + m_{\text{radionuclide}} \quad (\text{A3.3})$$

In this case $m_{\text{projectile}}$ and m_{target} are the masses of the proton (= 1.007825 amu) and the natural rubidium target (^{85}Rb and ^{87}Rb) also in atomic mass units, respectively. The emitted particle depends on the type of reactions that take place in the interaction between the target and the proton. So, in that case the mass of the ejected particle m_{ejectile} can be a neutron (= 1.008665 amu), proton or alpha particles (= 4.03298 amu). The mass of the radionuclide produced in the reaction is given by $m_{\text{radionuclide}}$. The speed of light c is expressed in MeV (= 931.5 MeV). The Q-value is expressed in MeV.

The mass related quantities used in this work were all taken from the Internet page designed by the Los Alamos group. All the values used were taken from the data tables of Moller *et al.* [Mol95] and from the publication of Audi and Wapstra [Aud95]. The calculated Q-values for the reactions are given in Chapter 4.

APPENDIX A4

CALCULATION OF CROSS-SECTION MEASUREMENTS AND PRODUCTION YIELDS

There are two important parameters that govern the calculation of production cross-sections and yields. These parameters are the rate of production (R_{ni}) of a particular radioisotope and the rate at which that radioisotope decays (A_i) known as the activity. The rate at which a particular radioisotope is produced is given [Fri81] by

$$R_m = \frac{dN}{dt} = N_0 I \sigma \quad (\text{A4.1})$$

Where N is the number of nuclei of a radioisotope

N_0 is the number of target nuclei per unit area in a foil ($/\text{cm}^2$)

I is the number of protons per unit time incident on the foil (s^{-1})

σ_i is the cross-section for the production of the radioisotope (cm^2)

The number of target nuclei in a foil and the proton flux are expressed as

$$N_0 = \frac{\Delta x N_A}{A},$$

$$I = \frac{I_t}{t_b} = \frac{K_1 C_t}{t_b}$$

Where N_A is Avogadro's number (mol^{-1})

Δx is the target thickness (g/cm^2)

C_t is the integrated charge given in μAh , $K_1 = 2.24719 \times 10^{16}$

A is the atomic mass of the target (g/mol)

I_t is the total number of protons incident on the target foil

t_b is the bombardment time (s)

The activity of the radioisotope is given by

$$A_i = -\frac{dN}{dt} = \lambda N \quad (\text{A4.2})$$

Where $\lambda = \frac{\ln 2}{T_{1/2}}$ is known as the decay constant and is expressed in terms of the half-life

$T_{1/2}$ of the radioisotope.

The activity A_i varies with time during the experiment whilst the rate of production during bombardment is assumed to stay constant. After bombardment, the radioactive species continue to decay according to the decay law

$$A_i(t) = A_{0i} \exp(-\lambda t) \quad (\text{A4.3})$$

Where A_{0i} is the activity at the start of irradiation, time $t = 0$

A4.2 Built-up of decay rate

Before deriving the formulas, we need to define the points in time of the experiment.

$t_0 = 0$ is the start of bombardment,

t_1 is the end of bombardment (EOB),

t_2 is the start of the counting time and

t_3 is the end of counting time

Where $t_3 > t_2 > t_1 > t_0$.

From the above points in time we deduce that

$t_1 - t_0 = t_b$ is bombardment time

$t_2 - t_1 = t_d$ is decay time

$t_3 - t_2 = t_c$ is counting time

After bombardment, the induced activity $A_i(t_1)$ of the radioisotope at time t_1 decays with time according to:

$$A_i(t) = A_i(t_1) \exp(-\lambda(t-t_1))$$

Therefore

$$A_i(t_1) = A_i(t) \exp[-\lambda(t_1-t)] \quad (\text{A4.4})$$

The activity $dA_i(t)$ produced in a small time interval dt at a particular point in time t during bombardment is given by

$$dA_i(t) = \lambda R_i dt \quad (\text{A4.5})$$

At the end of bombardment the activity $dA_i(t)$ decays to a value $dA_i(t_1)$ by

$$dA_i(t_1) = \lambda R_i dt \exp[-\lambda(t_1-t)], \quad 0 \leq t \leq t_1 \quad (\text{A4.6})$$

Integrating (A4.6) over the interval $t = 0$ to $t = t_1$ we get the total activity $A_i(t_1)$ at EOB,

$$A_i(t_1) = R_i [1 - \exp(-\lambda t_1)] \quad (\text{A4.7})$$

During the counting period, the instantaneous activity equals the average activity at a certain point in time t_m known as the “mean” time. Hence, the corresponding average activity is obtained by integrating dN (the number of disintegrations in time dt) over counting time $t = t_2$ to $t = t_3$ and dividing by $t_c = t_3 - t_2$. Therefore

$$A_i(t_m) = A_i(t_2) \exp[-\lambda(t_m - t_2)] = \frac{N}{t_3 - t_2} \quad (\text{A4.8})$$

Also we can express N as

$$\frac{N}{t_3 - t_2} = \frac{A_i(t_2)}{t_3 - t_2} \int_{t_2}^{t_3} \exp[-\lambda(t - t_2)] dt \quad (\text{A4.9})$$

Where $t_2 \leq t \leq t_3$. It follows from (A4.8) and (A4.9) that

$$t_m = t_2 - \frac{1}{\lambda} \ln \left[\frac{\exp(-\lambda t_2) - \exp(-\lambda t_3)}{\lambda(t_3 - t_2)} \right] \quad (\text{A4.10})$$

A4.3 Cross-section

The same mean activity can be obtained from the photo-peak area of a γ -line A_p obtained from the multi-channel analyzer Silena (EMCAPLUS version 1.04.1) which is used at the NAC

$$A_i(t_m) = \frac{A_p}{t_c \varepsilon_E \varepsilon_\gamma} \quad (\text{A4.11})$$

Where ε_E is the detector efficiency

ε_γ is the branching ratio.

From (A4.1) the cross-section is expressed as

$$\sigma = \frac{R_i}{N_o I} \quad (\text{A4.12})$$

Therefore by using equations (A4.11), (A4.12), (A4.10), (A4.7) and (A4.4) we can express the cross-section σ_i as

$$\sigma = \frac{A_p t_b}{t_c \varepsilon_\gamma \varepsilon_E N_o I_t [1 - \exp(-\lambda t_b) \exp(-\lambda(t_m - t_b))]} \quad (\text{A4.13})$$

A4.4 Production Yield

It follows from (A4.1) that the differential rate of production in units of (Bq/(MeV.μAh)) is given by the relationship

$$\frac{\Delta A}{\Delta R} = \lambda \quad (\text{A4.14})$$

where ΔA is the change in the rate of decay of a radioisotope and ΔR is the change in the rate of production of a radioisotope. From the definition of R in (equation A4.1) and I_0 it follows that

$$\Delta A = \frac{\lambda N_A I_0 \sigma}{A} \cdot \frac{\Delta E}{S(E)} \quad (\text{A4.15})$$

where $N_0 = (N_A dx)/A$ and A is the atomic mass of the target. Also I_0 is given by $I_0 = C_t K_1$ so that if ΔA is divided by ΔE it gives the yield as

$$R_{diff} = \frac{\Delta A}{\Delta E} = \left[\frac{\lambda N_A K_1 \sigma}{AS(E)} \right] \quad (\text{A4.16})$$

Where A is the atomic mass of the target material and $S(E)$ is the stopping power of protons discussed in APPENDIX 2. E denotes the average energy given by

$$E_{av} = (E_{in} + E_{out})/2 \quad (\text{A4.17})$$

E_{in} and E_{out} are the incident and exit energies, respectively.

A4.5 Thick target yield

The differential production rate in (A4.16) is a function of energy, hence, the rate of production R_{thick} for a particular radioisotope in a thick target where the beam is stopped is given by

$$R_{thick}(E_{in}) = \int_0^{E_{in}} R_{diff}(E) dE, \quad (\text{A4.18})$$

Calculated thick target production rates presented in this work were obtained as a function of energy by numerical integration of the particular differential production-rate curve up to that energy. The production rate $R_{thick}(E_{in}, E_{out})$ in a specific interval ($E_{in}-E_{out}$) was given by

$$R_{thick}(E_{in}, E_{out}) = R_{thick}(E_{in}) - R_{thick}(E_{out}) \quad (\text{A4.19})$$

A4.6 Computer Program

The cross-section and thin and thick target yield calculations were carried out by means of a computer program SIGMA and YIELD.

APPENDIX A5

IMPORTANT PARAMETERS USED IN THE ALICE-IPPE CODE

The production of medical radioisotopes used worldwide requires the evaluation of both experimental and modeled cross-sections for radionuclide production reactions. Generally, theoretical models are used only when measured cross-section data are not available or when there are large discrepancies between available experimental data sets. In most cases modeling is used as guide rather than full evaluation. In this work, the ALICE-IPPE code was solely used as black box to calculate theoretical cross-sections for comparison purposes. In general, this code is based on the nuclear reaction theories and models which covers the target-projectile and energy range including the pre-equilibrium model. ALICE can cover a wide range of values, but most of them are not relevant in this work, only cross-sections. Hence, only a few parameters were of importance in this study and they are described in below.

Table A5.1: Input parameters for the code ALICE-IPPE and their values used in this work

Variable	Value
AP	1
At	Target mass number
ZP	1
ZT	Target charge
NA	Max. of 9
NZ	Max. of 4
M3	4
QVAL	Reaction Q-value
ED	0.2
PLD	9
LDOPT	2

where

AP/AT Masses of the incident particle and of the target material, respectively

ZP/ZT	Charge of the incident particle and of the target, respectively
NA/NZ	Number of neutrons and incident particles out
M3	Neutron, proton, alpha and deuteron emission
Q-VAL	Reaction Q-values
ED	Energy bin mesh size in MeV
LDOPT	Ignatyuk level density
PLD	Level density parameter



APPENDIX A6

TABLES OF MEASURED CROSS-SECTIONS AND PRODUCTION RATES

Table A6.1 Approximate cross-sections for ^{22}Na and $^{62,65}\text{Zn}$.

Proton energy (MeV)	^{22}Na		Proton energy (MeV)		^{62}Zn		^{65}Zn	
	Cross-section (mbarn)		Cross-section (mbarn)		Cross-section (mbarn)		Cross-section (mbarn)	
99.46	18.3	± 1.1	37.88		13.1	± 1.3	7.63	± 0.51
95.13	18.6	± 1.1	34.53		18.8	± 1.7	7.76	± 0.52
90.66	19.1	± 1.1	30.88		32.2	± 2.5	8.86	± 0.59
86.66	19.4	± 1.2	27.51		53.7	± 4.0	10.4	± 0.70
82.51	19.7	± 1.2	23.78		71.3	± 5.2	13.6	± 0.91
78.21	20.1	± 1.3	21.64		67.0	± 4.7	15.5	± 1.1
73.73	20.9	± 1.4	19.31		54.4	± 3.9	21.6	± 1.5
69.79	20.2	± 1.4	16.76		34.2	± 2.4	40.2	± 2.7
66.47	22.4	± 1.5	13.87		8.50	± 0.69	93.6	± 6.3
64.78	23.5	± 1.3	10.43		-	-	200	± 14.
61.28	25.2	± 1.5	5.792		-	-	179	± 12.
57.62	28.2	± 1.8	-		-	-	-	-
53.78	32.4	± 2.0	-		-	-	-	-
49.71	37.8	± 2.4	-		-	-	-	-
46.44	41.9	± 2.6	-		-	-	-	-
42.98	43.4	± 2.7	-		-	-	-	-
40.44	40.3	± 2.6	-		-	-	-	-
38.55	32.9	± 1.9	-		-	-	-	-
35.22	20.0	± 1.2	-		-	-	-	-
31.64	5.40	± 0.34	-		-	-	-	-
28.33	0.58	± 0.055	-		-	-	-	-
24.70	0.086	± 0.011	-		-	-	-	-

Table A6.2 Cross-sections measured for the production of ^{82}Sr and its main radio-contaminants in the bombardment of ^{nat}Rb with protons.

Proton energy (MeV)	Cross-section (mbarn)									
	^{80}Sr	^{81}Sr	^{82}Sr	^{83}Sr	$^{85\text{m}}\text{Sr}$	^{85}Sr	^{86}Sr	^{87}Sr	^{88}Sr	^{89}Sr
100.1	1.53 ± 0.33	7.24 ± 0.80	31.1 ± 4.4	31.0 ± 3.1	3.68 ± 0.41	13.2 ± 1.2				
95.83	2.23 ± 0.43	7.36 ± 0.87	29.6 ± 2.9	32.9 ± 3.3	3.95 ± 0.44	13.6 ± 1.3				
91.38	2.35 ± 0.43	7.79 ± 0.94	32.8 ± 3.7	37.8 ± 3.7	3.91 ± 0.43	17.5 ± 1.6				
87.40	2.66 ± 0.48	8.13 ± 1.0	34.2 ± 3.8	39.6 ± 3.7	4.77 ± 0.53	15.1 ± 1.4				
83.29	2.58 ± 0.47	8.04 ± 1.1	36.5 ± 3.8	45.0 ± 4.2	5.19 ± 0.57	17.1 ± 1.6				
79.02	1.98 ± 0.43	11.1 ± 1.5	40.8 ± 4.2	51.0 ± 4.9	5.67 ± 0.63	19.0 ± 1.8				
74.57	1.63 ± 0.39	13.0 ± 1.7	41.7 ± 4.4	66.0 ± 6.4	6.10 ± 0.68	18.6 ± 1.8				
70.67	0.95 ± 0.30	14.9 ± 2.0	46.4 ± 4.8	73.1 ± 7.1	6.66 ± 0.74	22.2 ± 2.2				
67.37	-	18.6 ± 2.5	54.4 ± 5.5	75.9 ± 7.1	6.63 ± 0.74	22.0 ± 2.2				
65.69	-	16.7 ± 1.7	55.6 ± 5.2	81.3 ± 7.5	5.77 ± 0.60	28.0 ± 2.6				
62.23	-	14.0 ± 1.4	67.0 ± 6.2	91.0 ± 8.4	6.59 ± 0.67	26.9 ± 2.5				
58.61	-	9.47 ± 1.0	77.0 ± 7.2	84.4 ± 7.6	7.31 ± 0.74	31.0 ± 2.8				
54.82	-	3.25 ± 0.48	98.9 ± 9.1	93.9 ± 8.5	7.71 ± 0.77	34.9 ± 3.2				
50.82	-	-	123 ± 11	111 ± 10	9.15 ± 0.91	42.3 ± 3.9				
47.60	-	-	112 ± 10	167 ± 15	9.17 ± 0.86	47.7 ± 4.4				
44.21	-	-	94.7 ± 8.9	220 ± 20	12.2 ± 1.1	65.6 ± 6.0				
41.72	-	-	64.9 ± 6.2	285 ± 26	15.5 ± 1.4	86.7 ± 8.0				
39.48	-	-	31.5 ± 3.2	321 ± 29	22.5 ± 1.9	116 ± 10				
36.15	-	-	9.54 ± 1.2	333 ± 30	31.6 ± 2.7	148 ± 13				
32.64	-	-	2.01 ± 0.34	230 ± 20	41.0 ± 3.5	176 ± 16				
29.42	-	-	-	63.2 ± 5.9	37.7 ± 3.3	148 ± 13				
25.90	-	-	-	2.10 ± 0.31	23.5 ± 2.1	91.4 ± 8.4				
22.72	-	-	-	-	10.9 ± 1.0	47.2 ± 4.5				
20.49	-	-	-	-	9.27 ± 0.83	38.9 ± 3.8				
18.06	-	-	-	-	13.3 ± 1.2	56.6 ± 5.4				
15.35	-	-	-	-	28.8 ± 2.6	122 ± 11				
12.21	-	-	-	-	101 ± 8.9	281 ± 25				
8.287	-	-	-	-	188 ± 16	375 ± 33				

Table A6.3 Cross-sections measured for the production of Rb isotopes in $^{nat}\text{Rb}+p$.

Proton energy (MeV)	Cross-section (mbarn)									
	^{79}Rb	$^{81\text{m}}\text{Rb}$	^{81}Rb	^{82}Rb	^{83}Rb	$^{84\text{m}}\text{Rb}$	^{84}Rb	^{85}Rb	^{86}Rb	
100.1	47.3 ± 4.8	50.4 ± 4.8	93.8 ± 8.3	74.1 ± 6.9	57.8 ± 5.1	50.9 ± 4.5	129 ± 12.	35.2 ± 5.2		
95.83	54.1 ± 5.5	52.8 ± 6.4	97.6 ± 8.6	77.5 ± 7.2	60.0 ± 5.3	54.0 ± 4.8	131 ± 11.	36.5 ± 3.6		
91.38	61.0 ± 6.2	63.5 ± 7.8	102 ± 9.1	83.5 ± 7.8	63.2 ± 5.6	56.2 ± 5.1	139 ± 13.	38.6 ± 4.4		
87.40	74.0 ± 7.7	54.9 ± 7.1	99.5 ± 8.8	87.7 ± 7.9	65.2 ± 5.9	58.2 ± 5.4	144 ± 13.	38.3 ± 4.4		
83.29	75.7 ± 8.1	66.5 ± 8.7	106 ± 9.5	92.6 ± 8.4	71.1 ± 6.5	60.6 ± 5.8	142 ± 13.	40.5 ± 4.4		
79.02	64.9 ± 7.5	71.2 ± 9.6	117 ± 11	98.9 ± 9.1	77.5 ± 7.2	65.1 ± 6.3	154 ± 14.	44.4 ± 4.8		
74.57	35.8 ± 4.9	72.7 ± 9.5	126 ± 12	96.1 ± 9.0	80.6 ± 7.6	67.8 ± 6.7	153 ± 14.	42.7 ± 4.6		
70.67	21.6 ± 4.8	81.0 ± 10.	147 ± 14	97.9 ± 9.3	88.0 ± 8.4	68.3 ± 6.9	159 ± 15.	45.3 ± 4.9		
67.37	12.0 ± 4.6	89.6 ± 13.	148 ± 14	98.8 ± 9.5	91.9 ± 8.7	72.0 ± 7.4	171 ± 16.	45.6 ± 4.7		
65.69	-	70.3 ± 7.7	145 ± 13	99.9 ± 9.2	92.9 ± 8.1	55.7 ± 4.9	163 ± 14.	46.1 ± 4.5		
62.23	-	52.5 ± 6.1	129 ± 11	107 ± 9.8	97.0 ± 8.5	58.3 ± 5.2	171 ± 15	42.5 ± 4.3		
58.61	-	49.7 ± 6.3	99.4 ± 8.8	127 ± 12.	100 ± 8.8	64.8 ± 5.8	163 ± 14.	42.1 ± 4.3		
54.82	-	25.7 ± 3.7	49.8 ± 4.6	134 ± 12.	92.8 ± 8.3	65.6 ± 5.9	162 ± 14.	45.1 ± 4.6		
50.82	-	-	13.6 ± 1.3	105 ± 9.6	103 ± 9.2	68.8 ± 6.3	168 ± 15.	44.0 ± 4.5		
47.60	-	-	3.50 ± 0.4	70.5 ± 6.5	110 ± 9.9	55.1 ± 4.9	157 ± 14.	45.8 ± 4.6		
44.21	-	-	0.61 ± 0.2	38.8 ± 3.6	143 ± 13.	53.8 ± 4.9	152 ± 14.	46.3 ± 4.7		
41.72	-	-	0.17 ± 0.1	13.4 ± 1.3	172 ± 16.	52.2 ± 4.8	144 ± 13.	50.2 ± 8.5		
39.48	-	-	-	3.09 ± 0.4	198 ± 17.	61.0 ± 5.3	149 ± 15.	44.7 ± 8.2		
36.15	-	-	-	1.26 ± 0.20	201 ± 18.	61.5 ± 5.4	144 ± 14.	48.0 ± 8.2		
32.64	-	-	-	-	194 ± 17.	72.5 ± 6.3	166 ± 16.	53.3 ± 7.1		
29.42	-	-	-	-	123 ± 11.	73.5 ± 6.4	164 ± 15.	43.1 ± 6.1		
25.90	-	-	-	-	32.8 ± 3.2	64.1 ± 5.7	148 ± 14.	40.6 ± 5.8		
22.72	-	-	-	-	2.17 ± 0.33	59.0 ± 5.3	141 ± 13.	28.9 ± 3.9		
20.49	-	-	-	-	0.59 ± 0.16	43.5 ± 3.9	111 ± 10.	19.2 ± 3.1		
18.06	-	-	-	-	0.73 ± 0.24	24.9 ± 2.3	64.5 ± 6.2	8.88 ± 1.8		
15.35	-	-	-	-	-	7.70 ± 0.75	21.1 ± 2.2	2.47 ± 0.8		
12.21	-	-	-	-	-	0.74 ± 0.11	2.01 ± 0.3	-		
8.287	-	-	-	-	-	0.16 ± 0.10	0.68 ± 0.2	-		

Table A6.4 Cross-sections measured for the production of Br and Kr isotopes in $^{nat}Rb+p$.

Proton energy (MeV)	^{77}Br		^{80m}Br		^{79}Kr		Cross-section (mbarn)
100.1	20.4	± 2.1	3.77	± 0.56	50.9	± 5.0	
95.83	20.9	± 2.2	3.78	± 0.54	46.9	± 4.7	
91.38	21.5	± 2.2	4.27	± 0.62	42.1	± 4.3	
87.40	21.8	± 2.1	3.57	± 0.41	33.4	± 3.3	
83.29	20.0	± 2.0	3.20	± 0.39	26.6	± 2.7	
79.02	15.6	± 1.6	3.24	± 0.40	20.5	± 2.2	
74.57	7.76	± 0.89	2.90	± 0.37	16.6	± 1.8	
70.67	3.89	± 0.56	2.52	± 0.30	16.9	± 1.9	
67.37	1.23	± 0.26	2.24	± 0.29	17.7	± 1.9	
65.69	1.01	± 0.38	1.97	± 0.26	19.6	± 2.3	
62.23	0.55	± 0.21	1.82	± 0.25	23.9	± 2.6	
58.61	-		1.77	± 0.26	30.2	± 3.2	
54.82	-		-		32.5	± 3.2	
50.82	-		-		26.7	± 2.7	
47.60	-		-		17.3	± 1.9	
44.21	-		-		6.83	± 0.98	
41.72	-		-		1.96	± 0.60	
39.48	-		-		3.09	± 0.4	
36.15	-		-		1.26	± 0.20	

Table A6.5 Calculated thin target yield for ^{82}Sr based on the excitation function.

Proton energy (MeV)	Cross-section (mbarn)	Yield (mCi)($\mu\text{Ah}\cdot\text{MeV}$)	
		Rb	RbCl
100.1	31.1	0.00898	0.00589
95.83	29.6	0.00839	0.00551
91.38	32.8	0.00899	0.00591
87.40	34.2	0.00900	0.00592
83.29	36.5	0.00936	0.00616
79.02	40.8	0.00996	0.00656
74.57	41.7	0.00976	0.00645
70.67	46.6	0.0104	0.00690
67.37	54.4	0.0119	0.00788
65.69	55.6	0.0124	0.00821
62.23	67.0	0.0141	0.00930
58.61	77.0	0.0170	0.0112
54.82	98.9	0.0198	0.0130
50.82	123	0.0225	0.0149
47.60	112	0.0197	0.0131
44.21	94.7	0.0161	0.0107
41.72	64.9	0.0106	0.00702
39.48	31.5	0.00491	0.00325
36.15	9.54	0.000138	0.0000913
32.64	2.01	0.000267	0.0000177

Table A6.6 Calculated thick target yield of ^{82}Sr based on the excitation function.

Proton energy (MeV)	Cross-section (mbarn)	Yield (mCi/ μAh)	
		Rb	RbCl
100.1	31.1	0.778	0.515
95.83	29.6	0.741	0.491
91.38	32.8	0.703	0.465
87.40	34.2	0.667	0.442
83.29	36.5	0.629	0.416
79.02	40.8	0.588	0.389
74.57	41.7	0.544	0.360
70.67	46.6	0.505	0.333
67.37	54.4	0.468	0.309
65.69	55.6	0.446	0.295
62.23	67.0	0.402	0.266
58.61	77.0	0.346	0.228
54.82	98.9	0.279	0.184
50.82	123	0.193	0.127
47.60	112	0.124	0.0819
44.21	94.7	0.0634	0.0417
41.72	64.9	0.0299	0.0196
39.48	31.5	0.01000	0.00659
36.15	9.54	0.00204	0.00134

REFERENCES

- [And77] Andersen H. H. and Ziegler J. F. Hydrogen stopping power and ranges in all elements. In *The Stopping and Ranges of Ions in Matter* (Ed. Ziegler J. F.), Vol. 3, pp. 1. Pergamon, New York (1977).
- [Aud95] Audi G. and Wapstra A. H. *Nuclear Physics*. A595, pp. 409 (1995).
- [Bes77] Besenbacher F. Energy straggling for protons and Helium ions. *Phys. Lett.* Vol. 61A, No. 1 (1977).
- [Bey89] Beyer G. J. Spallation produced radioisotopes for nuclear medical application. *Isotopenpraxis*, No. 25, pp. 2-10 (1989).
- [Bla75] Blann M. Pre-equilibrium decay. *Ann. Rev. Nucl. Sci.*, 25, 123 (1975).
- [Bla89] Blann M. Pre-compound decay models for medium energy reactions. *Transactions-for-the-American-Society*, CONF-891103-(CONF891103) Vol. 60, pp. 260-261 (1989).
- [Blo77] Blokhin A. I., Ignatyuk A. V., Lunev V. P., Pronyaev V. G. Integral contribution of direct processes inelastic scattering spectra and the pre-equilibrium decay model. INIS-mf--4468 (INISmf4468), pp. 130-134 (1977).
- [Cac93] Cackette M. R., Ruth T. J. and Vincent J. S. ^{82}Sr production from metallic Rb targets and development of an ^{82}Rb generator system. *Appl. Radiat. Isot.* Vol. 44, No. 6, pp. 917-922 (1993).
- [Chu76] Chu W. K. Calculation of energy straggling for protons and Helium ions. *Phys. Rev. A*, Vol. 13, No. 6 (1976).
- [Dep90] Deptula C., Khalkin V. A. Excitation functions and yields for medically important generators $^{82}\text{Sr} - ^{82}\text{Rb}$, $^{123}\text{Xe} - ^{127}\text{I}$ and $^{201}\text{Bi} - ^{201}\text{Pb} - ^{201}\text{Tl}$ obtained with 100 MeV protons. *Nukleonika*, Vol. 35, No. 1-3 (1990).
- [Fri81] Friedlander G. *Nuclear and Radiochemistry*, 3rd Edition, New York (1981).
- [Hel83] Helus F. *Radionuclides Production*, Vol. II, CRC Press (1983).
- [Hod97] Hodgson P., Gadioli H and Gadioli E. *Introductory Nuclear Physics*, Clarendon Press, Oxford (1997).
- [Hop87] Hoppes D. D., Coursey B.M., Schima F. J. National Bureau of Standards decay-scheme investigation of strontium-82-rubidium-82. *Appl. Radiat. Isot.* Vol. 38, No. 3, pp. 195-203 (1987).

- [Hor80] Horiguchi T., Nome H., Yoshizawa Y. Excitation functions of proton-induced nuclear reactions on ^{85}Rb . *Int. Jour. Appl. Radiat. Isot.* Vol. 31, pp. 141-151 (1980).
- [Jan82] Janni J.F. Proton range-energy tables, 1 keV-10 GeV. *Atomic and Nuclear Data Tables*, Vol. 27, No 1 and 2 (1982).
- [Jud87] Judge S. M., Woods M. J. A partial decay scheme study of ^{82}Rb and consequences for radiation dose measurements. *Appl. Radiat. Isot.* Vol. 38, No. 3, pp. 185-190 (1987).
- [Kno89] Knoll G. F. Radiation Detection and Measurements, 2nd Edition, New York (1989).
- [Lag92] Lagunas-Solar M. C. Radionuclide production with >70-MeV proton accelerator: current and future prospects. *Nucl. Instr. and Meth. in Phys. Res.* **B69**, pp. 452-462 (1992).
- [Lag93] Lagunas-Solar M. C. and Haff R. P. Theoretical and experimental excitation functions for proton-induced nuclear reactions on $Z = 10$ to $Z = 82$ target nuclides. *Radiochimica Acta* **60**, pp. 57-67 (1993).
- [Mau87] Mausner L. F. Production of ^{82}Sr by proton irradiation of RbCl . *Appl. Radiat. Isot.* Vol. 38, No. 3, pp. 181-184 (1987).
- [Mil92] Mills S. J., Steyn G. F and Nortier F. M. Experimental and theoretical excitation functions of radionuclides produced in proton bombardment of copper up to 200 MeV. *Appl. Radiat. Isot.* Vol. 43, No 8, pp. 1019-1030 (1992).
- [Mol95] Moller P., Nix J. R., Myers W. D. and Swiatecki W. J. Nuclear Ground-State Masses and Deformations. *Atomic Data and Nuclear Data Tables* **59**, pp. 185-381 (1995).
- [Nee79] Need J. A survey of some applications of cyclotron. *IEEE Transactions on Nuclear Science*, Vol. NS-26, No. 2, April 1979.
- [Nor90] Nortier F. M. Considerations concerning targetry for radioisotopes production at the NAC and the production of ^{67}Ga , ^{111}In and ^{109}Cd . Ph. D thesis (1990).
- [Now81] Nowotny R. Calculation of proton-induced radioisotope production yield with a statistical-model based code. *Int. Jour. Appl. Radiat. Isot.* Vol. 32, pp. 73-78 (1981).
- [Oka88] Okamoto K. Influence of target and sample properties on nuclear data measurements. *IAEA, INDC (NDS)-213/G+ M3*, October 1988.

- [Oka89] Okamoto K. Monitor reactions for the production of radioisotopes for medical use. *IAEA, INDC (NDS)-195/GZ*, January 1989.
- [Qai82] Qaim S. M. Nuclear data relevant to cyclotron produce short-lived medical radioisotopes. *Radiochimica Acta* **30**, pp. 147-162 (1982).
- [Reu83] Reus U. Westmeier W. Atomic and Nuclear data tables, Vol. 29, No. 1 and 2 (1983).
- [Sch89] Schwerer O. Cross-sections for monitor reaction for radioisotope production. *IAEA, INDC (NDS)-218/GZ+*, December 1989.
- [Ste90] Steyn G. F., Mills S. J., Nortier F. M. *et al.* Production of ^{52}Fe via proton-induced reactions on manganese and nickel. *Appl. Radiat. Isot.* Vol. 41, No. 3, pp. 315-325 (1990).
- [Tho87] Thomas K. E. Strontium-82 production at Los Alamos National Laboratory. *Appl. Radiat. Isot.* Vol. 38, No. 3, pp. 175-180 (1987).
- [Ver93] Verashchagin Y. I. Cyclotron ^{82}Sr production for medical application. *Nucl. Instr. Meth. Phys. Res.* **A334**, pp. 246-248 (1993).
- [Yan76] Yano Y. Development of positron emitting radionuclides for imaging with improved positron detector. *IAEA, SM-210/123* (1976).
- [Zai91] Ziatseva N. G. *et al.* Cross-sections for 100 MeV proton-induced nuclear reactions and yield of some radionuclides used in nuclear medicine. *Radiochimica Acta* **54**, pp. 57-72 (1991).